TAACOS: Phase I FUV Report

Date:	April 2, 2002
Document Number:	COS-11-0016
Revision:	Revision A
Contract No.:	NAS5-98043
CDRL No.:	N/A

Prepared By:
S. Penton, COS Software Scientist, CU/CASA — Date

Reviewed By:
I. Becker, COS Software Consultant, BATC — Date

Reviewed By:
D. Ebbets, COS Software Consultant, BATC — Date

Reviewed By:
S. Beland, COS Software Engineer, CU/CASA — Date

Approved By:
K. Brownsberger, COS Sr. Software Scientist, CU/CASA — Date

Approved By:
Jim Green, COS Principal Investigator — Date

Approved By:
Erik Wilkinson, COS Scientist — Date

Approved By:
John Andrews, COS Experiment Manager — Date

Center for Astrophysics & Space Astronomy
University of Colorado
Campus Box 593
Boulder, Colorado 80309

REVISIONS

Letter	ECO No.	Description	Check	Approved	Date
-		Initial Release			
A	COS-071	FUV pixel size change			

Original Release Name:	Date
Drawn: S. Penton	6-27-00
Reviewed:	
Approved:	

THE UNIVERSITY OF COLORADO
At Boulder
The Center for Astrophysics and Space Astronomy

TAACOS: Phase I FUV Report

Size	Code Indent No.	Document No.	Rev
A		COS-11-0016	A
Scale: N/A			

TABLE OF CONTENTS

TABLE OF FIGURES

TABLE OF TABLES

1. SCOPE

The purpose of the Target Acquisition Analysis for the Cosmic Origins Spectrograph (TAACOS, see COS-08-0011) is to ensure that the algorithms and procedures defined in COS OP-01, IN0090-619, IN0090-623 and COS-FSW-001 are sufficient to accurately place a science target of interest at a proper location in the aperture in a timely and efficient fashion. The target acquisition (TA) requirement is that the science target should be aligned to within ±0.3" (45 km/s) in the dispersion direction in the 3σ case. The cross-dispersion requirement is only that the target spectra should be fully contained in the predicted detector subarray. An offset error of 3 (25μm) cross-dispersion pixels is ~0.3", which we adopt as our cross-dispersion TA goal. There exists an additional science requirement of allowing for TAs with accuracies of ±0.1" (15 km/s) in the dispersion direction in the 3σ case for special observations. Phase I of the TAACOS analysis is designed to provide an initial evaluation for all TA phases for the FUV gratings. The Phase I goal is to determine if the proposed algorithms are viable to center the targets with the desired accuracies. We will also propose improvements to the initial TA strategy, which should allow FUV observations to routinely achieve the stricter ±0.1" accuracy for both dispersion and cross-dispersion target centering. Recommend changes to the flight software (FSW) will be given in COS-11-0014. This document does not address other proposed TA methods such as centering the target using an imaging mode on the NUV channel. A future report will discuss these options and Phase I TA using the near ultraviolet (NUV) detector. Phase II of the TAACOS project will expand the targets tested. For further details of the TAACOS project, see COS-08-0011 or http://cos-arl.colorado.edu/TAACOS.

1.1 BACKGROUND

HST/COS TAs are planned to be performed spectroscopically without the aid of sky images[1]. This type of TA is more complicated than imaging TAs, and new procedures have been described to spectroscopically acquire targets with COS. To test these new TA procedures a COS simulator has been developed that can produce a detector image for any grating, target location, and input spectra. This document describes the FUV simulator, and the lessons learned from simulating the TA procedures. The simulator and the analysis are performed using ray-tracing and other software developed using the Interactive Data Language (IDL) at CU/CASA. This effort relies heavily on ground-based estimations of the COS in-orbit performance. Final TA algorithms will be tested during the integration and testing (I&T) phase of the COS development.

[1] As mentioned, there is the possibility of using the imaging mode of the COS NUV channel for TA. This option is explored is COS-11-0027 (TAACOS: Target Acquisition with the TA1 Mirror).".

1.2 FUV PHASE I: PROJECT OVERVIEW/EXECUTIVE SUMMARY

The FUV channel TA has been evaluated for the G130M, G160M, and G140L gratings.[2] For Phase I of this evaluation, we will restrict our analysis to the acquisition of an isolated quasi-stellar object (QSO) an $F_\lambda = 10^{-15}$ ergs/cm^2/s/Å using the 2.5" diameter primary science aperture (PSA). The redshift of the input spectra will be varied to illustrate certain TA pitfalls, which must be avoided. QSO targets with varying spectral index, and flux, crowded fields, and extended targets will be tested in Phase II. The Phase II analysis will be performed using both the PSA and the bright object aperture (BOA) at all planned aperture locations. This document describes the Phase I TAACOS evaluation analyses for all four phases of the TA process, Calibrate Aperture Location (LTACAL), Target Search (LTASRCH), Peakup in the Cross-Dispersion Direction (LTAPKXD), and Peakup in the Dispersion Direction (LTAPKD). The acronyms used to describe each of the TA phases are taken from the flight software subroutine names as described in the Control Section Flight Software Requirements Document (IN0090-619).

We find that the original, "stock", TA strategies will center isolated point sources to within the required accuracies (0.3"). However, our analysis have uncovered minor adjustments to these routines and strategies which will significantly improve the centering of FUV targets in the PSA. We find that routine FUV TAs should be able to acquire targets to within 0.1" in both dispersion (DD) and cross-dispersion (XD) in the 3σ case. This equates to a TA introduced 3σ wavelength error of <10.5 km/s for the medium resolution gratings, and <67 km/s for the G140L. TAs should take less than 30 minutes for a $F_\lambda=10^{-15}$ ergs/cm^2/s/Å QSO spectrum observed at S/N=40. Many TA strategies acquire targets to within 0.05" in both XD and DD.

For initial pointing errors less than 3", a 3x3x1.767" LTASRCH followed by a 2x2x1.767" LTASRCH appears to be the best TA strategy. This strategy should take ~18 minutes. However, for initial pointing errors larger than 3" this strategy fails to acquire targets accurately. A 4x4x1.767" LTASRCH followed by a 2x2x1.767" LTASRCH would acquire targets with initial pointing errors of up to 4.5" in about 28 minutes.

For initial pointing errors less than 1", we find that a 2x2x1.767" LTASRCH acquires about 99% of targets to within 0.1" in XD and DD. This TA would take about 7 minutes.

[2] The original version of this TER assumed an FUV "Y" pixel size of 15µm. To ensure that the electronic stim pulses would be in the correct digital range, the "Y" pixel sizes of the FUV detectors have been increased to 25µm. Revision A of this document addresses the minor changes that this has on TA. We find that this has no impact on the findings of the original report, except that some values, such as the cross-dispersion plate scales, have changed accordingly.

Following this LTASRCH with a second 2x2x1.767" LTASRCH or a LTAPKXD plus a LTAPKD (3x0.6") acquires 100% of targets to within 0.1" in XD and DD. These second phases would additional 6 minutes to the TA time.

We find that flux-centroiding is best method for the LTASRCH and LTAPKD phases. Using the mean cross-dispersion coordinate is sufficient in LTACAL and LTAPKXD.

Extraction subarrays that remove Geocoronal airglow lines are essential for TA. We do not see a need for moving extraction subarrays, which account for the motion of the target spectrum in the DD with motion in the aperture.

1.3 DOCUMENT OVERVIEW

In section 2, we list the applicable COS documentation related to this report. In section 3, we list the abbreviations and acronyms used in this document. In section 4, we will briefly review the FUV detectors, the coordinate systems used, the HST point spread function (PSF) at the COS science apertures, and current estimates of the COS FUV effective areas. In addition, we describe the input QSO plus geocoronal airglow spectra used for our TAACOS simulations, as well as the TA extraction sabarrays used in our TAACOS simulations. In section 5, we use our TAACOS FUV simulator to test the four target acquisition (TA) phases (LTACAL, LTASRCH, LTAPKXD, and LTAPKD) independently. In section 6, we test the TA phases as a package for eight TA scenarios. We test these packages against both a $3\sigma = 3$" and $3\sigma = 1$" initial pointing error distribution. In section 7, we briefly summarize our FUV TA findings.

2. APPLICABLE DOCUMENTS

The following documentation describes the algorithms and procedures proposed for HST/COS target acquisition. The referenced documents are of the revision in effect on the date of the release of this document.

COS-08-0011	TAACOS: Target Acquisition Analysis for the COS (CASA)
COS-11-0014	Recommended TA FSW and Operations Changes, based upon the TAACOS Phase I Reports for the FUV and NUV Channels
COS-11-0017	TAACOS: Detector Summary Images
COS-11-0027	TAACOS: Target Acquisition with the TA1 Mirror
COS-FSW-001	Target Acquisition Concepts for COS (BATC)
COS-SYS-022	Current Estimates of COS Sensitivity
COS-OP-01	COS Science Operations Requirement Document (CASA)
IN0090-619	Control Section Flight Software Requirements Document for the COS (BATC)
IN0090-623	Software Design Document for the Control Section Flight

ST-ICD-02E	Axial Scientific Instruments to Optical Telescope Assembly and Support Systems Module (STSCI)

3. LIST OF ACRONYMS AND ABBREVIATIONS

ACS	Aperture Coordinate System
BATC	Ball Aerospace & Technologies Corp.
BOA	Bright Object Aperture
BOP	Bright Object Protection
CAL	Calibrate Aperture Location
CASA	Center for Astrophysics and Space Astronomy
CDR	Critical Design Review
COS	Cosmic Origins Spectrograph
CU	University of Colorado @ Boulder
DD	Dispersion Direction (X)
DCS	Detector Coordinate System
FC	Flux Centroid
FFC	Floored (threshold) Flux Centroid
FOS	Faint Object Spectrograph
FSW	Flight SoftWare
FUSE	Far Ultraviolet Spectroscopic Explorer
FUV	Far UltraViolet
GSC II	Guide Star Catalog II (STSCI)
HST	Hubble Space Telescope
HVLOW	LOW High Voltage state
HVNOM	NOMinal High Voltage state
IC	Image Coordinate system
IDL	Interactive Data Language
I&T	Integration and Testing
LTACAL	TA subroutine for the Location of the CALibration lamp spectra
LTAPKD	TA subroutine for the PeaKup in the Dispersion direction
LTAPKXD	TA subroutine for the PeaKup in the cross(X)-Dispersion direction
LTASRCH	TA subroutine for target Locating with a (spiral) target SeaRCH
m	minute
NUV	Near UltraViolet
p	Pixel
PSF	Point Spread Function (of HST)
PtNe	Platinum-Neon (Wavelength Calibration Lamp)
PSA	Primary Science Aperture
QSO	Quasi-Stellar Object
RTB	Return To Brightest

s	second
TA	Target Acquisition
TAACOS	TA Analysis for COS
TS	(Spiral) Target Search
UCB	University of California at Berkeley
X_f	Final DD target location (ACS)
X_0	Initial DD target location (ACS)
XD	Cross-Dispersion (Y) direction
XDL	cross(X) Delay Line (microchannel plates)
Y_f	Final XD target location (ACS)
Y_0	Initial XD target location (ACS)

4. FUV DETECTOR OVERVIEW AND PERFORMANCE ANALYSIS

4.1 BACKGROUND AND THE FUV DETECTOR COORDINATE SYSTEM

The COS FUV detector consists of two cross delay-line (XDL) microchannel plates. Each of these segments contain an active area of 85x10mm, with a < 9mm gap between the segments. The longer axis, X, is the dispersion direction (DD), and the shorter axis, Y, is the cross-dispersion (XD) direction. Detector electronics digitize photon events into 16384x1024 pixels per segment. Electronic stimulation pulses (E-stims or stim pulses) are inserted into the detector images to track changes in the physical detector coordinate system (DCS) with respect to the image coordinates (IC). The electronics associated with the E-stims will determine what subarray of the 16384x1024 IC system will map to the active DDL detector regions. Figure 1 displays the detector segments in the DCS and gives the bandpasses for the three FUV gratings (G130M, G160M, & G140L). The FUV pixel sizes are assumed to be 6x25 µm.

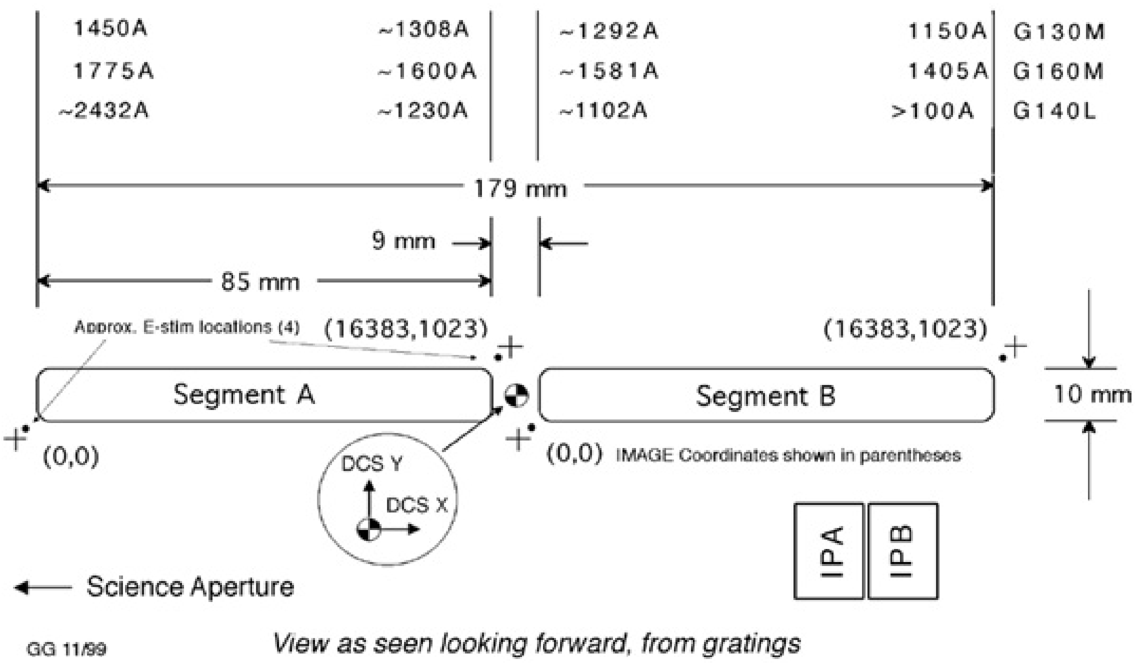

Figure 1: FUV Detector Coordinate System. This figure details the spectral coverage of the FUV gratings as well as the physical dimensions of the two FUV segments. This figure was taken from the CDR presentation of Oswald Siegmund (4/26-27/2000).

4.2 THE HST POINT SPREAD FUNCTION AND THE COS SCIENCE APERTURES

The primary driver to the COS TA algorithms is the relationship between the size of the point spread function (PSF) of HST and the COS aperture at the aperture location. Current ray-tracing codes indicate that the on-axis HST PSF is approximately symmetric with a radius of ~0.204mm (0.75"). It is important to remember that the HST beam is not focused at the aperture location. Figure 2 displays the HST PSF of a point source at the COS primary science aperture (PSA) in coordinates of millimeters and arcseconds on the sky. In this figure, the 2.5" diameter aperture is shown in red, while simulated photons from an isolated point source are shown in green. The hashed area indicates the aperture mechanism, which blocks photons not in the aperture. The PSA and the bright science aperture (BSA) are both 0.340mm (1.250") in radius. Therefore, the COS science apertures capture 100% of the HST PSF, plus an additional ~0.136mm (0.5") annulus (indicated by Δr in Figure 2).

The spatial relationship between the COS apertures and the HST PSF limits the accuracy of centering the target at the center of the aperture. For example, an off-axis mis-alignment of 0.5" in any direction will still produce the same number of counts (ignoring Poisson statistics) as a perfectly on-axis TA. TA methods that rely solely upon photon counts, such as flux-centroiding, will have difficulty to properly center a target with accuracies better than 0.5". Figure 3 shows an example of the HST PSF when the target is off-axis by 0.48" in dispersion and cross-dispersion direction. In this case, ~14% of the photons are vignetted producing a clear indication of target mis-alignment.

Figures 2 and 3 are TAACOS simulations of a monochromatic distant point source. Each simulation consists of ~1600 photons. No Geocoronal airglow lines have been included. If included, they would uniformly fill the aperture.

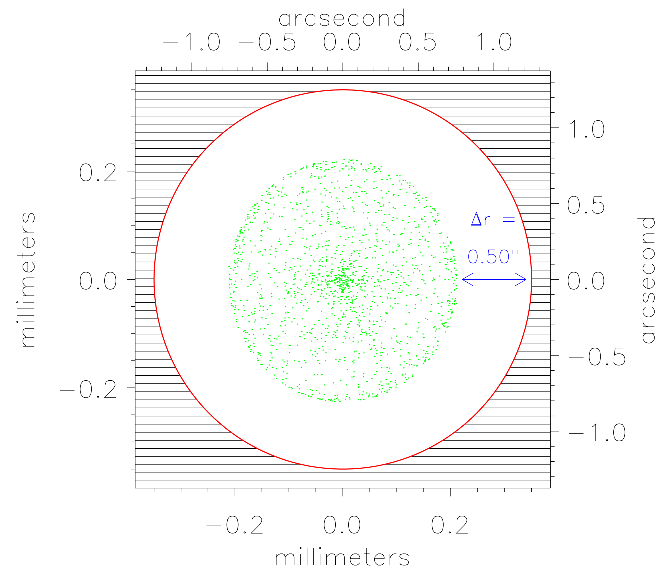

Figure 2: The HST PSF as compared to the COS PSA. The out of focus HST PSF is approximately circular with a radius of ~0.2 mm at the COS aperture mechanism. The COS PSA is circular with a radius of 0.34mm, which corresponds to 1.25" on the sky. The HST PSF is smaller than the COS PSA aperture by 0.136mm or ~0.5".

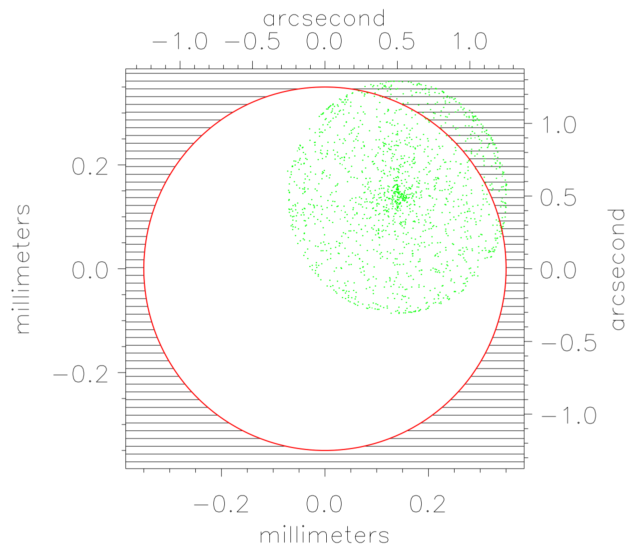

Figure 3: The HST PSF as compared to the COS PSA for an observation 0.48" offset in both X and Y. About 14% of the incoming light is vignetted by the aperture mechanism.

4.3 TAACOS: INPUT SPECTRUM

The TAACOS input spectrum for the majority of our modeling is based upon the faint object spectrograph (FOS) QSO composite spectrum (Zheng, et al. 1998, ApJ, 492, 855). The TAACOS FUV input spectrum differs from the FOS QSO composite spectrum in the following ways:

1) It has been scaled to an average flux level of $F_\lambda = 10^{-15}$ ergs/cm^2/s/Å This flux level is at the extreme low level of observability with HST+STIS, yet is likely to be the typical COS QSO brightness.

2) It has been adjusted to correspond to a target with z=0.125. This places intrinsic Lyα (1216Å) emission in the G130M bandpass, CIV (1550 Å) in the G160M bandpass, and both strong peaks in the G140L bandpass. We will also use spectra adjusted to other redshift to demonstrate pitfalls in some TA procedures.

3) Simulated non-physical absorption features are inserted into the spectrum at regular intervals ranging from equivalent widths of 2 Å to 2 mÅ. These spectral features are a convenient method for determining the sensitivity limits of COS observations.

4) Daytime or nighttime Geocoronal airglow lines are included as indicated in Table 1. Airglow fluxes in this table were derived by scaling Tables II and III from Meier (1991) to observed STIS values (Table 6.7 of the STIS Instrument Handbook). Nitrogen lines are not included, as it is assumed, based upon STIS experience that the Nitrogen scale is much less than Oxygen or Hydrogen. The daytime and nighttime intensities are in Rayleighs, R, where 1 R = 10^6 photons cm^{-2} s^{-1} $(4\pi$ sr$)^{-1}$. Airglow is much more a problem with COS than STIS/GHRS due to the large aperture and the absence of a spectroscopic slit. For our TAACOS simulations, the airglow is assumed to uniformly fill the aperture. The adopted values of Table 1 are only for the purpose of selecting appropriate TAACOS subarrays (section 4.11), and are not intended to simulate actual in-orbit flux levels, which are largely unknown.

Figures 4-6 display the input spectrum for the G130M, G160M, and G140L gratings, respectively. Because these input spectra are intended to simulate the actual spectra of a typical extragalactic science target, Geocoronal emission is not present in these figures. Subsequent detector images, which have a defined exposure time, include simulated daytime Geocoronal emission.

Table 1: Expected Geocoronal Airglow Lines

Geocoronal Airglow Line Line	Daytime Intensity in R	Nighttime Intensity in R
OI λ911	17	8.3
OI λ989	161	0.6
HI λ1025	571	2.7
OI λ1027	64	0
OI λ1152	28	0
HI λ1216	20000	2000
OI λ1304	2000	13
OI λ1356	204	12.5
OI λ2471	45	1

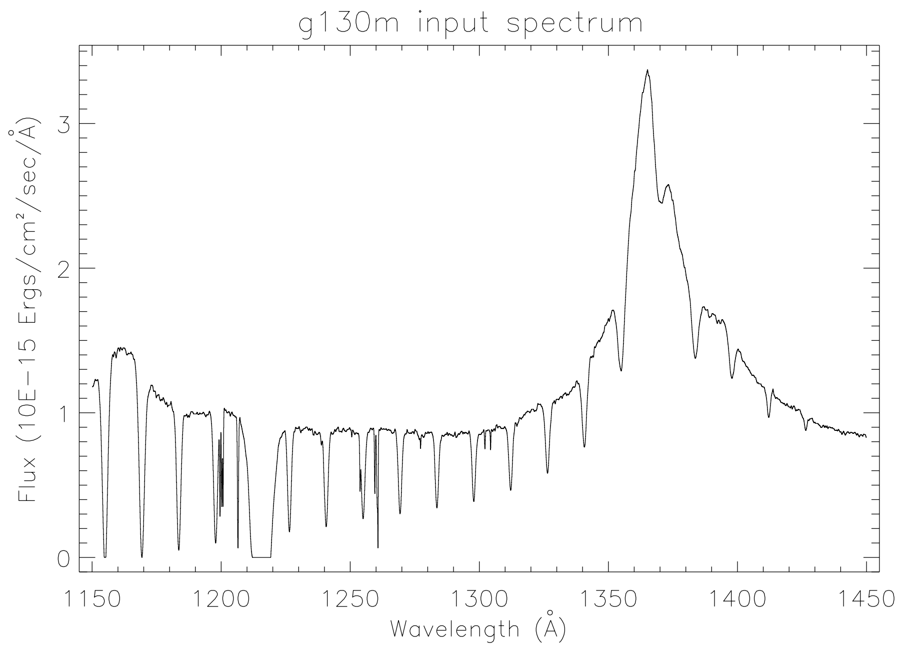

Figure 4: Input spectrum for the G130M target acquisition trials. This spectrum is the FOS composite QSO spectrum scaled to an $F_\lambda = 10^{-15}$ ergs/cm^2/s/Å. Additional "non-physical" features have been added to the spectrum as described in the text. Geocoronal Lyα has not been added to this spectrum. The 1350Å emission feature is Lyα (z=0.125).

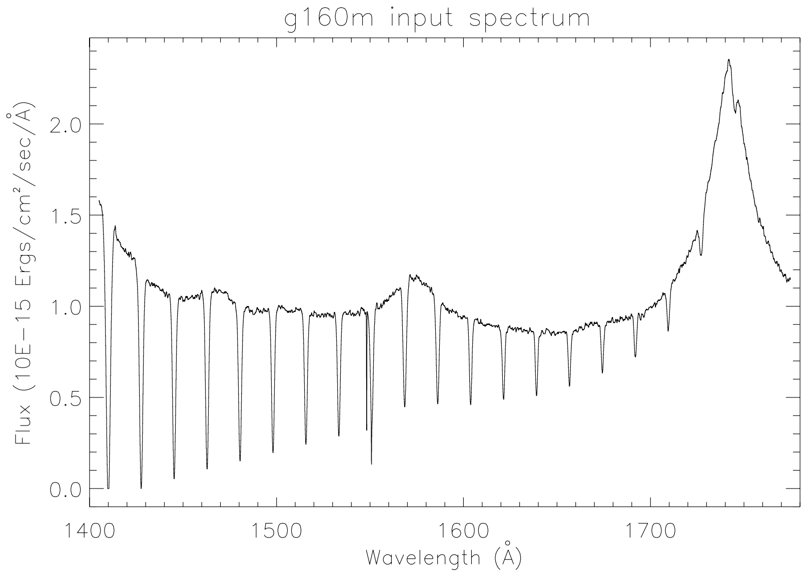

Figure 5: G160M input spectrum. This spectrum is the scaled FOS composite QSO spectrum with additional non-physical spectral features. The emission features at 1580Å and 1740Å are SIV λ1404 and λ CIV 1550 at z=0.125, respectively.

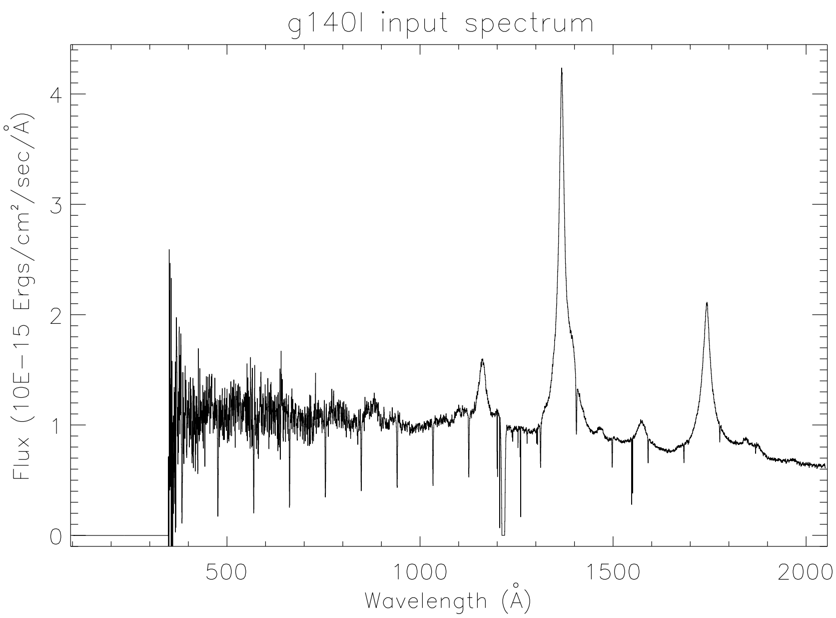

Figure 6: G140L input spectrum. This spectrum is the scaled FOS composite QSO spectrum with additional non-physical spectral features. The emission features of the previous two figures are visible, as well as Lyβ emission (1150Å) at z=0.125.

4.4 COS EFFICIENCES AND DETECTOR NOISE

The COS instrument (optics + detectors) efficiencies used for the FUV TA analysis are taken from (COS-SYS-022), and are current as of January 27, 2000. For convenience, these efficiency results are presented in Figure 7. For purposes of TA, we assume that the detectors will have a constant background rate of 0.5 counts s^{-1} cm^2. This rate is consistent to the in-flight count rate currently being detected by the Far Ultraviolet Spectroscopic Explorer (FUSE), which uses detectors nearly identical to the COS FUV detectors. This extremely low count rate equates to 4.25 counts s^{-1} per detector segment or about one count per pixel per month. Before being processed by the TAACOS simulator, the count rate corresponding to the input flux is determined using the effective area curves. Detector background events are added during the pixelization of the detector images (see Figures 9-11).

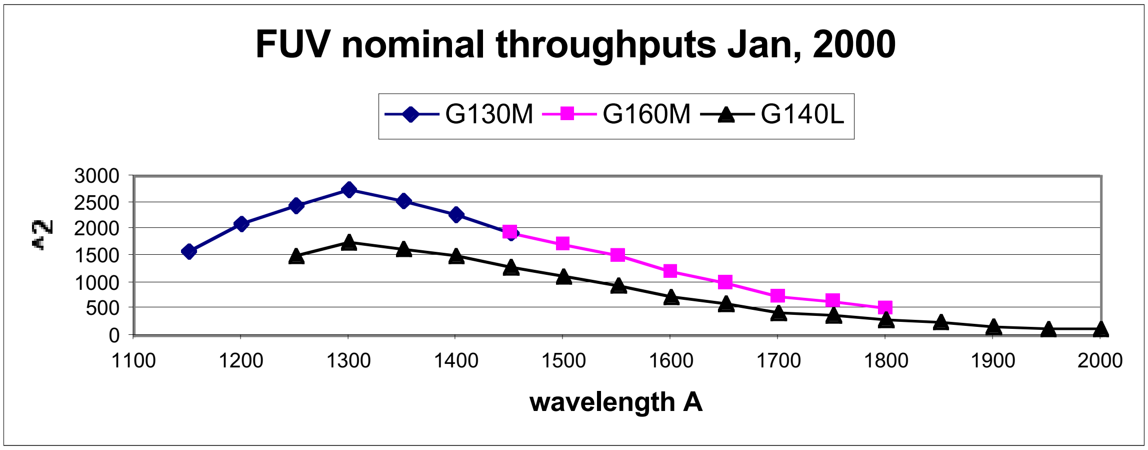

Figure 7: HST+COS FUV effective areas (in cm^2) as a function of wavelength. This figure was taken from COS-SYS-022.

4.5 EXPOSURE TIMES REQUIRED FOR S/N = 40 TARGET ACQUITIONS

With TAACOS, the TA phases (LTACAL, LTASRCH, LTAPKXD, and LTAPKD) have been performed for a variety of exposure times. We find that a signal-to-noise ratio (S/N) of 40 (~1600 target photons) is sufficient for all TA phases. This includes determining the cross-dispersion spectral location (LTACAL and LTAPKXD), and provides enough photons distributed by the PSF to perform count-based centering (LTASRCH and LTAPKD). Figure 8 below shows the exposure time required to achieve a S/N of 40 as a function of target flux in units of ergs/cm^2/s/Å. The required exposure times of the G130M and G160M are nearly identical, and are indicated by the red line. For a source with $F_\lambda = 10^{-15}$ ergs/cm^2/s/Å, the exposure time is ~30 seconds. For the G140L (shown in green), the exposure time for the same flux target is ~20 seconds. We will use exposures of these durations for the majority of our TAACOS trials.

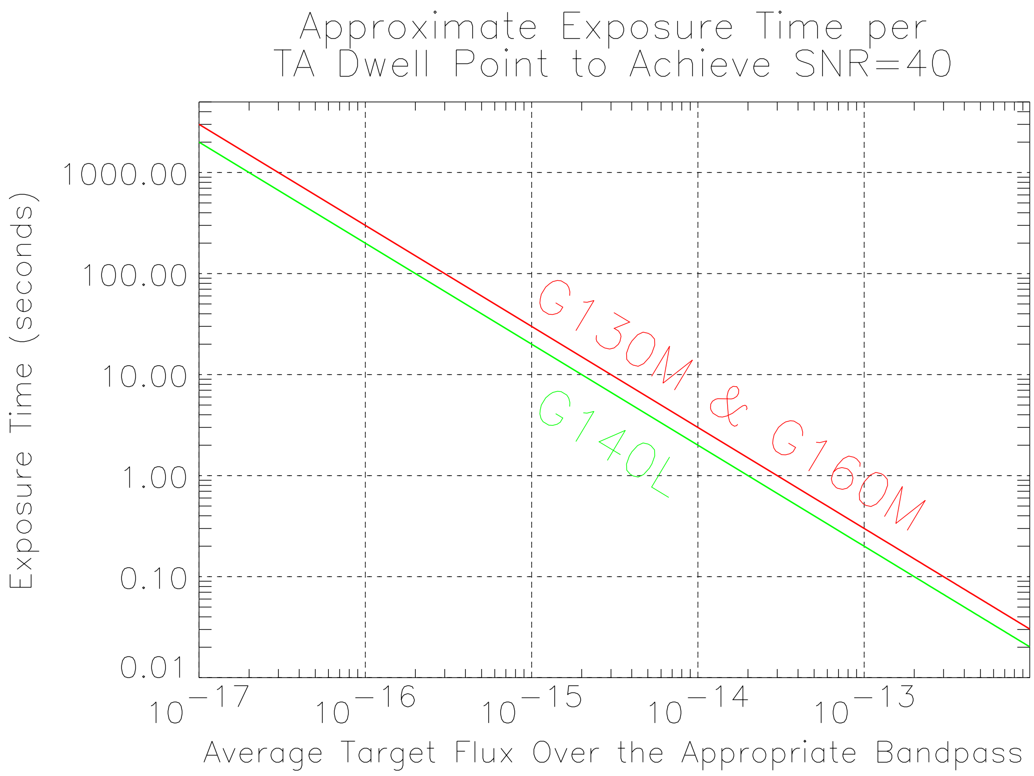

Figure 8: Approximate exposure time (in seconds) required to achieve a S/N of 40 for each grating as a function of input target flux in units of ergs/cm^2/s/Å.

4.6 DETECTOR BLURRING AND SIMULATED IMAGES

The FUV detectors produce charge clouds that are unique to each incoming photon energy and microchannel plate location. However, this also means that photons of the same energy and location will produce different cloud charges and detector locations. As such, no readout electronics can detect the incoming photon's physical location to better than this intrinsic "blurring". For the COS FUV detectors, the 1σ radial blurring is ~25μm in the DD and ~50μm in the XD (private communication, UCB detector scientists). This intrinsic blurring is added to each incoming photon to create an image of the FUV detector in physical space.

Detector images for the three FUV gratings are shown in Figures 9-11. Each of the detector images uses the input spectrum described in section 4.3, simulated for a 30-second exposure (20 seconds for the G140L). Daytime Geocoronal airglow lines have been included. Figures 9-11 contain two panels. The upper panel displays an image of the full detector, while the lower panel zooms in on the actual spectra. These detector images are in the detector coordinate system (DCS). Note that positive DCS X (dispersion direction) is to the left, placing FUV segment B on left. This orientation allows direct comparison between the detector images with the input spectra of Figures 4-6. The 9mm gap between the two FUV detector segments has been simulated in these detector images.

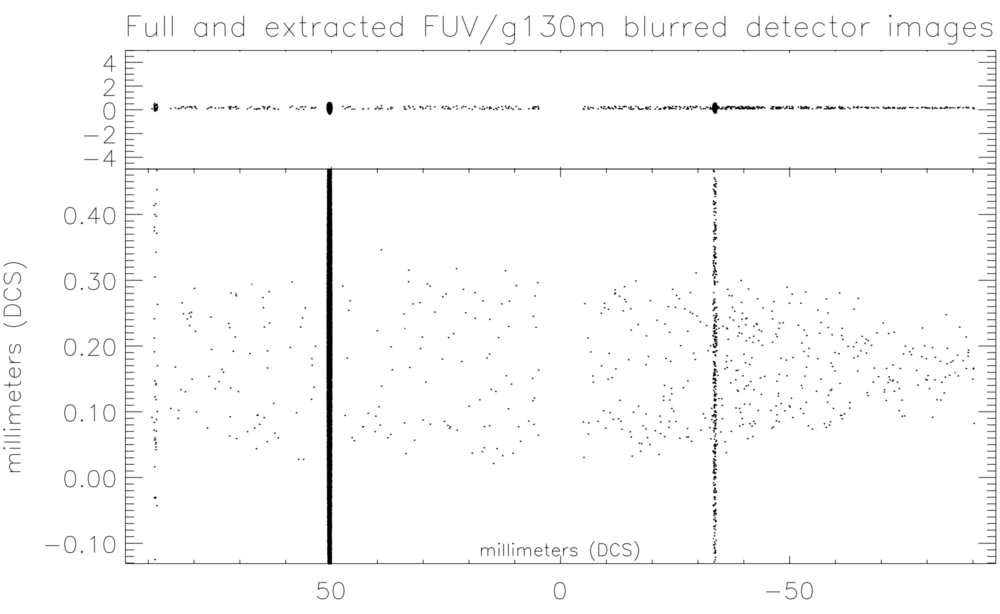

Figure 9: FUV full (Top) and extracted simulated daytime G130M blurred detector images. Note the simulated geocoronal airglow lines at the DCS dispersion coordinate of 50 (1216Å) and 32 (1356Å) mm, among others.

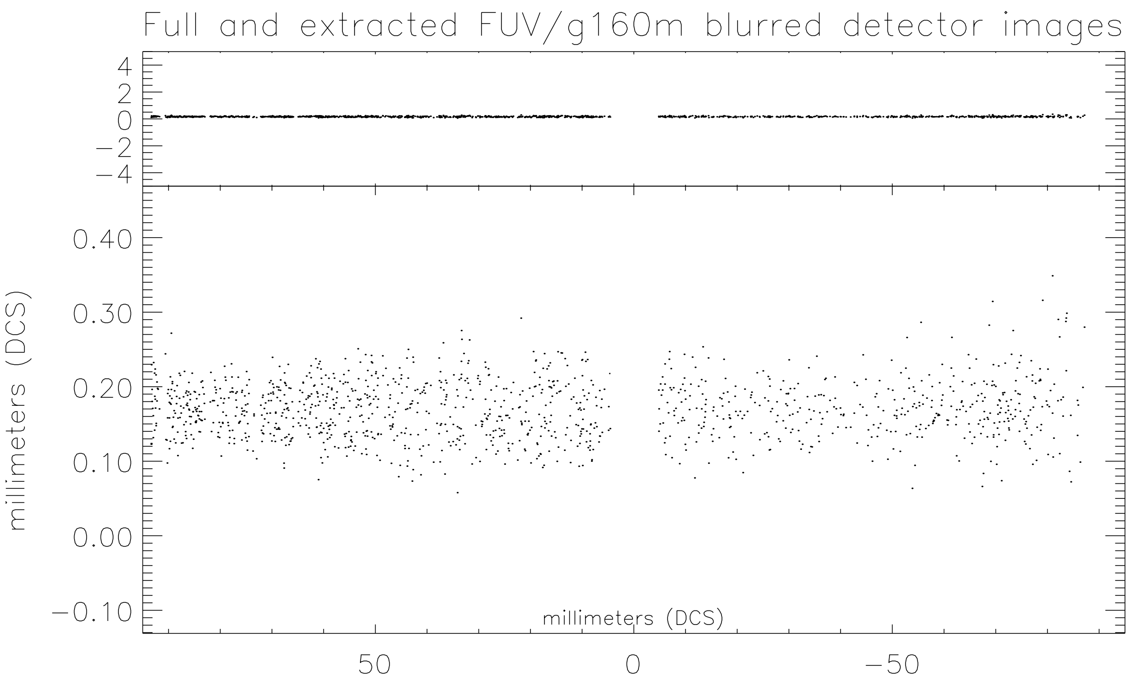

Figure 10: FUV full and extracted simulated 30-second G160M detector images**.**

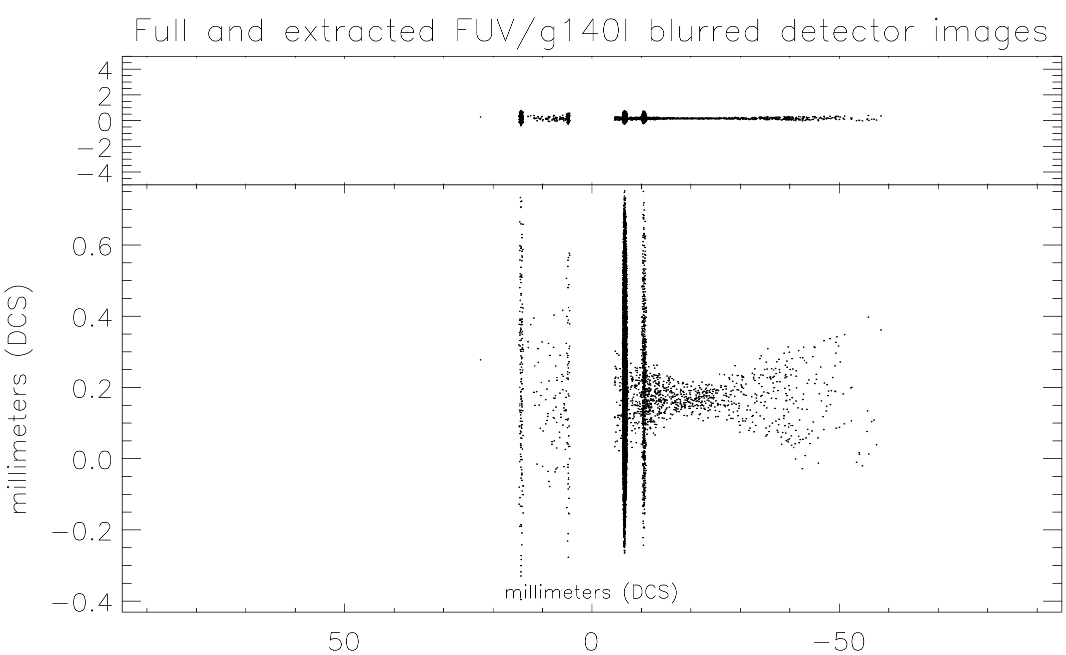

Figure 11: FUV full and extracted simulated 20-second daytime G140L detector images.

4.7 D/A CONVERSION AND EXTRACTION SUBARRAYS

Photon events from the FUV detector are converted to image coordinate (IC) “pixels” by the detector electronics over the range (0,0) - (16383,1023) on each segment. For the purposes of TAACOS, we assume that the active areas of the detector segments are limited to the central 14000x1000 IC pixels. The actual active area in IC will not be known until a flight XDL has been assembled and tested at UCB.

Depending on the flux of the target source, it is possible for the Geocoronal airglow emission lines to contribute more photon events than the science target. Airglow photons of a given wavelength are imaged on the detector based upon the HST entrance location and angle and uniformly fill the COS aperture. The airglow lines will have dispersion and cross-dispersion extents larger than point sources. Because the airglow lines uniformly fill the aperture, telescope motion during TA will not affect the location of emission lines in ICs. TAACOS simulations indicate that narrow airglow emission lines should have spatial extents of ~42 25μm cross-dispersion pixels (1 mm) and ~160 6μm dispersion pixels (1 mm). Due to the strong count rates and differing cross-dispersion profiles of airglow lines compared to point sources, areas of the detector which contain strong airglow lines should be masked out for TA to succeed.

This masking will be performed in FSW with two of the four subarrays allowed per detector segment. For the G130M, Lyα, OI λ1152, and OI λ1356 should be masked out (OI λ1304 lies on the detector gap). For the G160M, no strong geocoronal lines are present (OI lies on the gap). For the G140L, Lyβ, OI λ1027, OI λ1152, OI λ1304, and OI λ1356 should be masked out (Lyα lies on the gap). The uncontaminated portion of the G140L segment B is very modest. Therefore, TAACOS uses only segment A to perform target acquisition simulations. We recommend that this be the case for on-orbit TAs as well. Table 2 below gives the FUV detector segment and the approximate mean dispersion (<X>) DCS and approximate IC coordinates of these emission lines. Since the exact pixel size and DCS to IC mapping is not known at this time, these locations are at best approximations.

Table 2: DCS/IC Coordinates of Strong Geocoronal Lines

Grating	Airglow Line	<X> in DCS (mm)	<X> in IC (pixel)	FUV Segment
G130M	OI λ1152	88.45	15420	B
	Lyα	50.52	8805	B
	OI λ1356	-33.59	10526	A
G140L	OI λ1027	14.23	2480	B
	OI λ1152	4.82	840	B
	Lyβ	14.36	2502	B
	OI λ1304	-6.57	15239	A
	OI λ1356	-10.47	14559	A

4.8 FUV CROSS-DISPERSON PROFILES

Figures 12 and 13 below display the cross-dispersion (XD) profiles of the 30-second G130M and G160M trials. Figure 14 presents the cross dispersion profile of the 20-second G140L exposure. These profiles correspond to a target perfectly centered in the aperture. Off-axis cross-dispersion profiles vary significantly. Each figure contains a panel for each detector segment. Segment B is presented on the left to match the presentation of the input spectra and detector images. The cross-dispersion profiles are presented in terms of IC (pixels) and DCS (millimeters). Geocoronal emission has been excluded by using the appropriate sub-arrays. Note the bimodal distribution of the G130M XD profiles. Segment B of the G140L does produce enough counts to be useful for TA, and is not displayed.

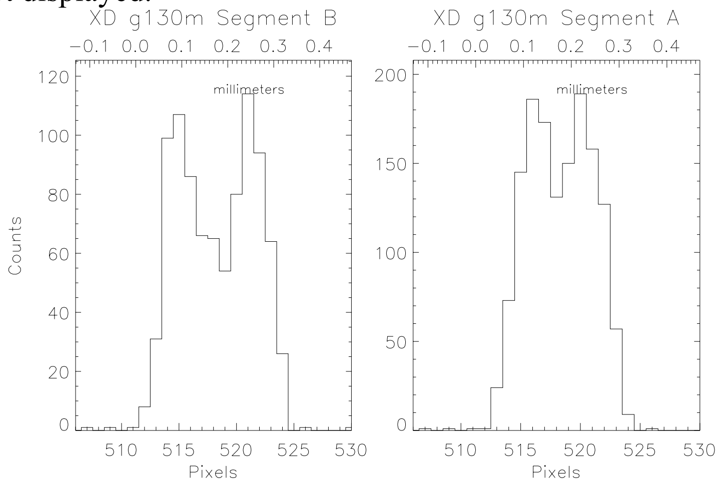

Figure 12: On-axis XD profiles of the FUV/G130M segments. The number of photons detected is shown for each cross-dispersion image coordinate (IC) pixel for a 30-second exposure. The upper axis gives the cross-dispersion detector location in the DCS (millimeters).

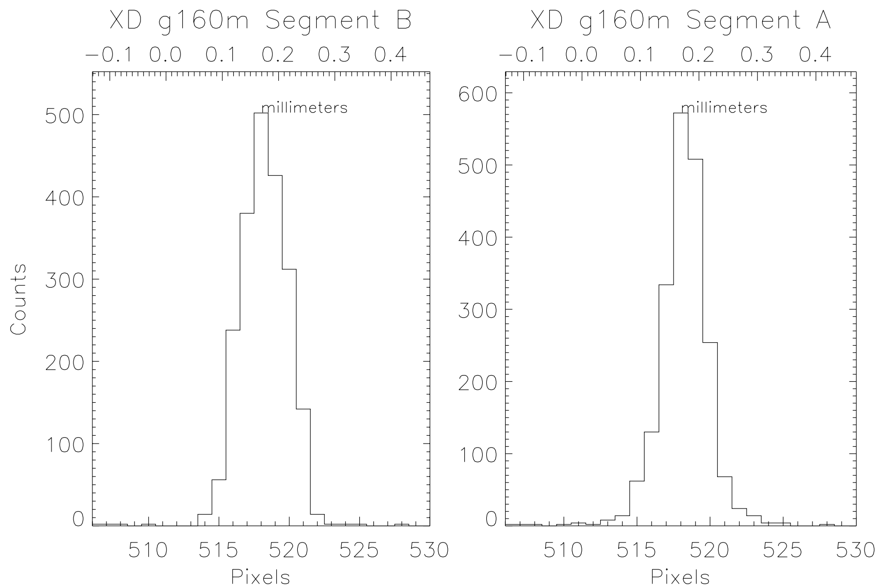

Figure 13: On-axis cross-dispersion (XD) profiles of the FUV/G160M segments. The simulated exposure time is 30-seconds.

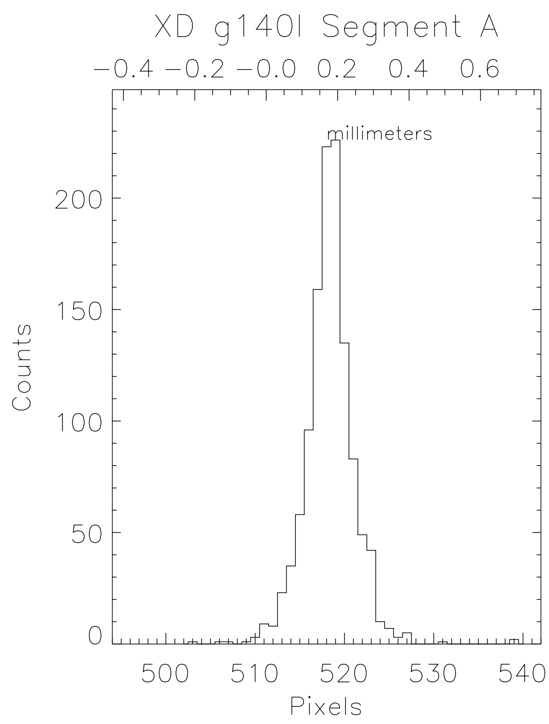

Figure 14: On-axis cross-dispersion (XD) profiles of the FUV/G140L segments. The simulated exposure time is 20-seconds.

4.9 OFF AXIS ALIGNMENT AND DETECTOR LOCATION

Target motion in the aperture displaces the spectral location on the detector in both the dispersion and cross-dispersion direction. Proper characterization of this motion is necessary for selection of the subarray sizes. To determine this relationship between aperture location and spectral location on the detector, TAACOS simulations were performed using emission line sources displaced over a 7x7x0.4" grid in the aperture. For each grating, four emission line wavelengths were selected near the bandpass edges of each detector segment. The dispersion and cross-dispersion aperture-detector coefficients (α_x and α_y in units of IC pixels (p) per arcsecond (")) were determined by linear least squares fits to the median location of the emission lines in the both directions.

Figures 15-17 display the results and mapping coefficients of each of the emission line trials. The left panels display the dispersion aperture-detector mappings in dispersion image coordinates (IC X) versus offset in the aperture for all 49 grid points. Each panel also gives the wavelength of the emission line and the linear least squares results of the aperture-detector mappings. The right panels give the cross-dispersion (Y) results. Each dwell points represents a 4 minute exposure of an $F_\lambda = 10^{-12}$ ergs/cm^2/s/Å emission line.

Combining the results of all four emission lines produces the final dispersion (α_x) and cross-dispersion (α_x) mapping coefficients for each detector listed in Table 3. These slopes (α_x and α_y) are a measure of the change of spectral location on the detector for a given translation in the aperture (see Figures 15-17). The errors in the coefficients are a measure of the change in the mapping in both directions, and the uncertainties introduced in using short exposure times. The larger errors in determining α_y are the result of the changing cross-dispersion profiles (see Figures 7-9), and is largest for the G140L grating.

Table 3: Aperture To Detector Mappings

Grating	Dispersion (α_x)	Cross-Dispersion (α_y)
G130M	α_x =-43.48 ± 0.24 p/"	α_y =9.02 ± 0.37 p/"
G160M	α_x =-42.92 ± 0.28 p/"	α_y =10.12 ± 0.23 p/"
G140L	α_x =-45.44 ± 0.14 p/"	α_y =9.48 ± 1.67 p/"

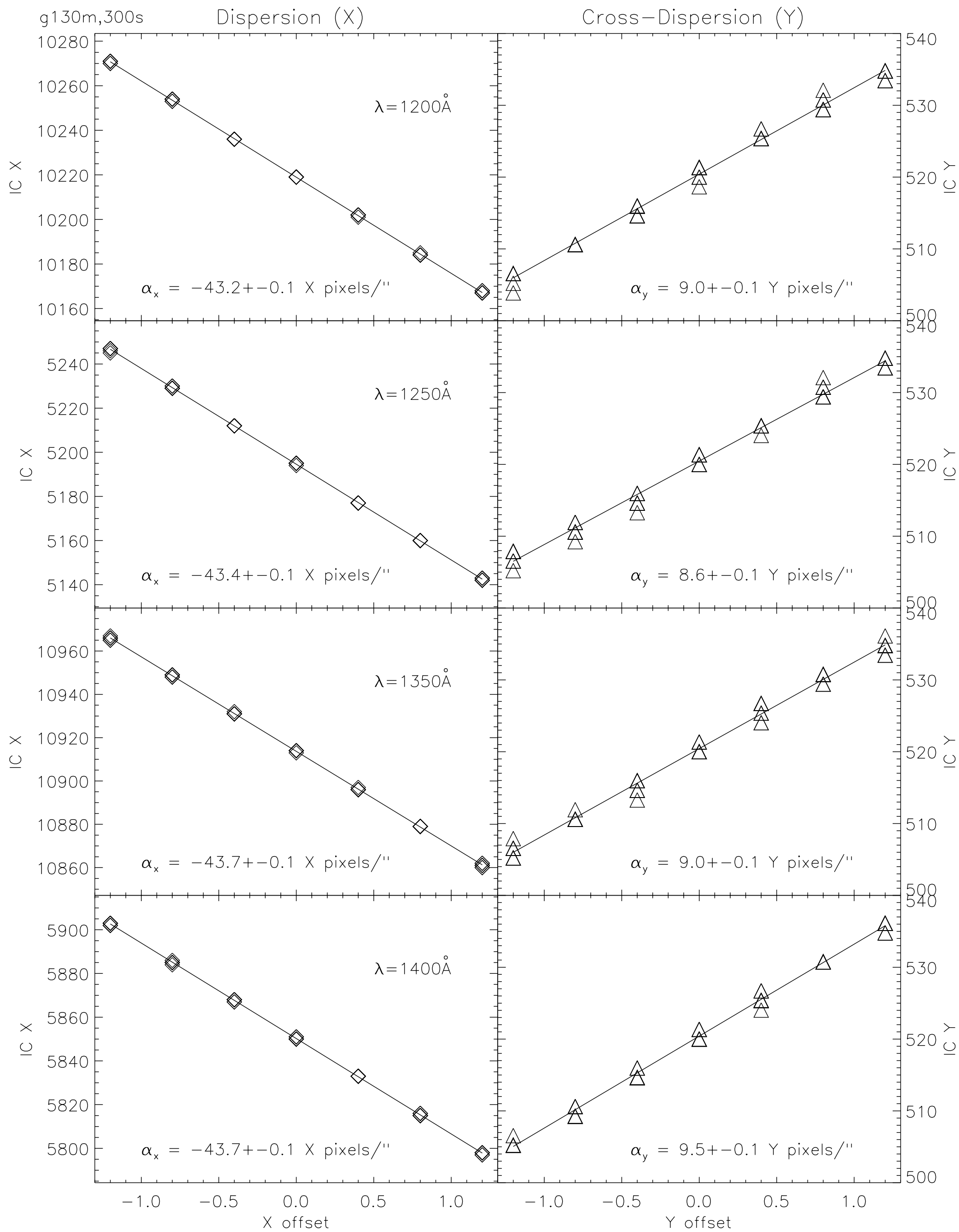

Figure 15: Aperture to detector location mapping for the G130M grating. The detector location in image coordinates (IC) is determined for each emission line over a grid of 7x7x0.4"x300s dwell points. The left column corresponds to the dispersion direction (X), the right column to the cross-dispersion direction (Y). The slopes of the position translation (α_x and α_y) determine the change of detector location for a given translation in the aperture.

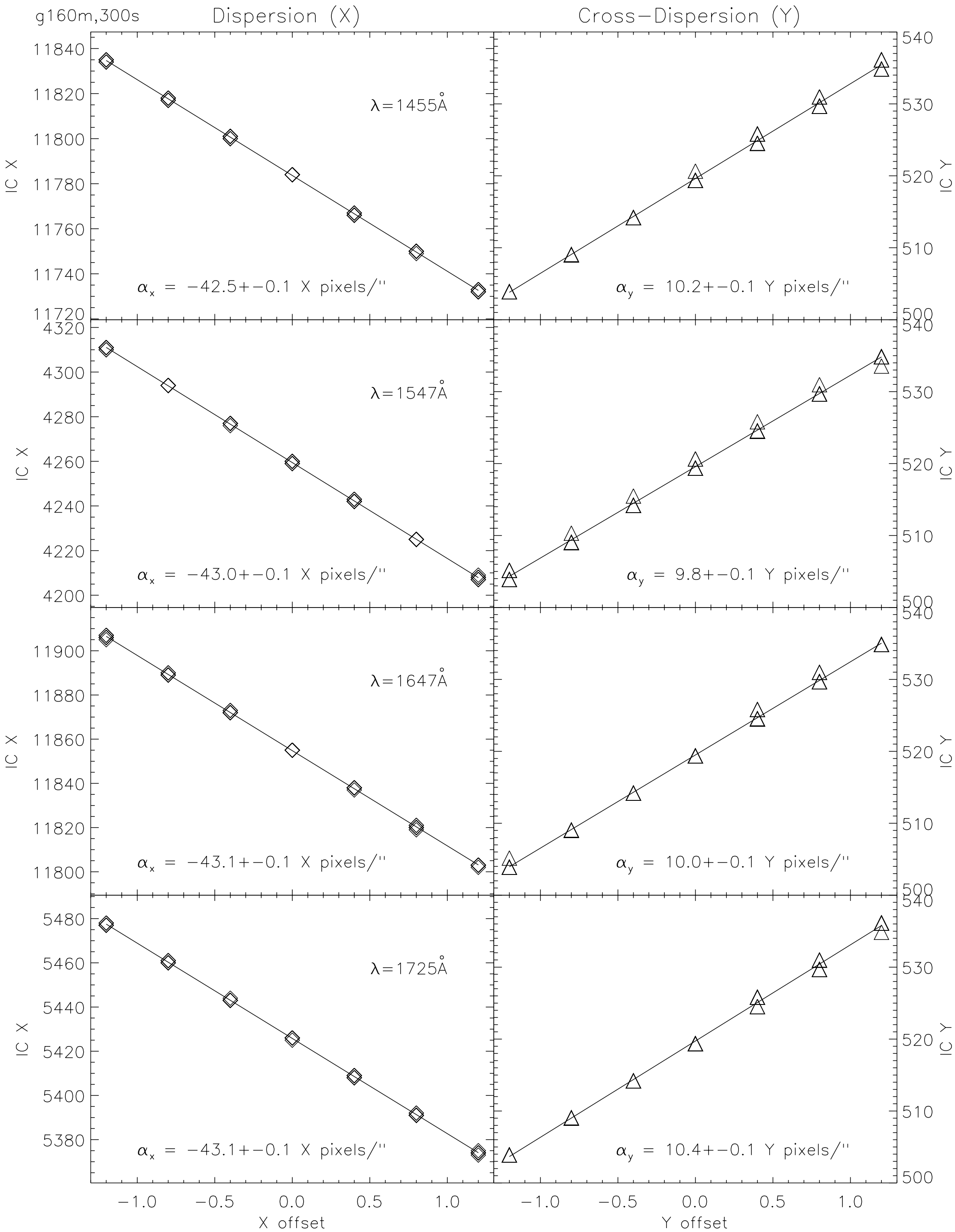

Figure 16: Aperture to detector location mapping for the G160M grating (see Figure 15)

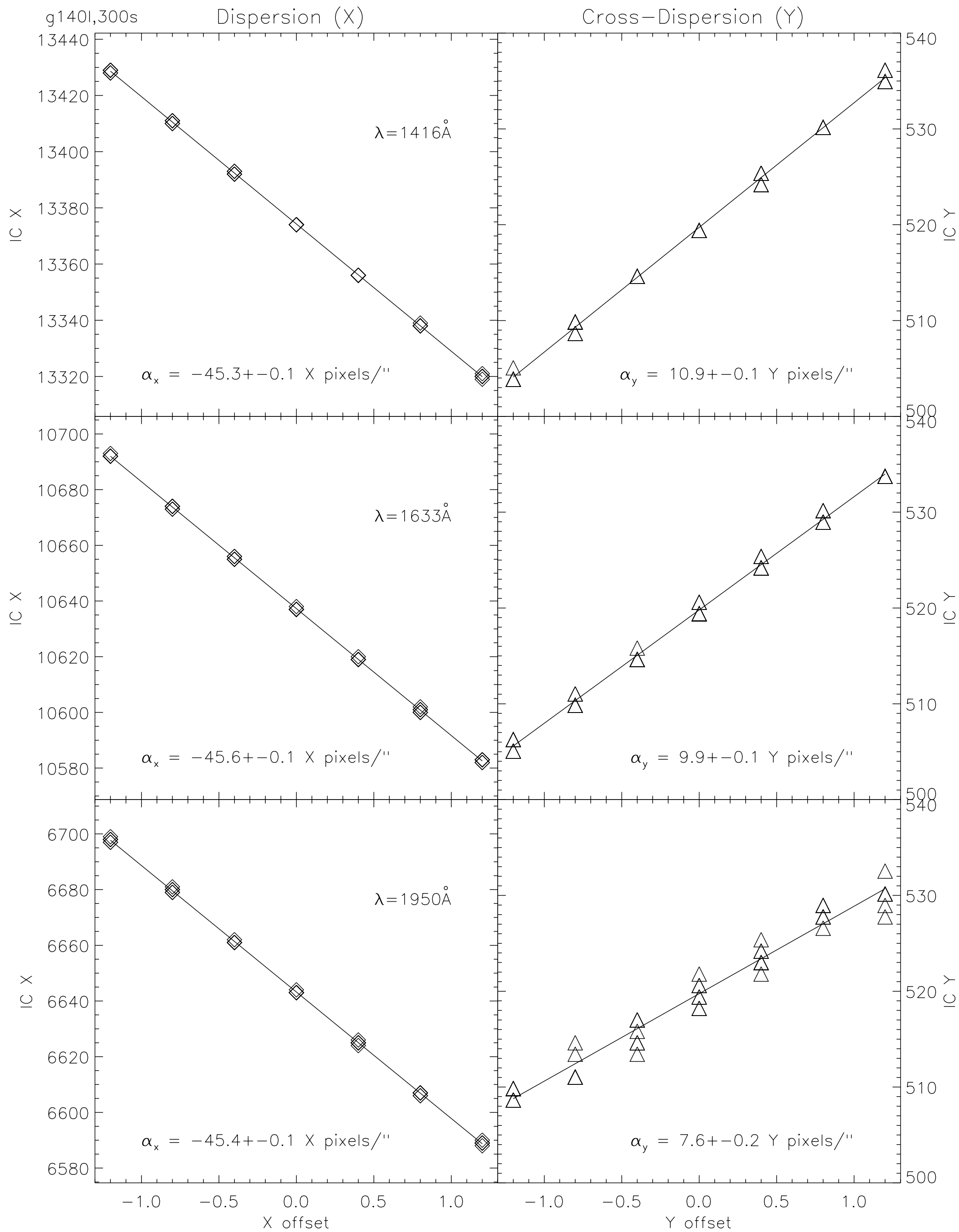

Figure 17: Aperture to detector location mapping for the G140L grating (see Figure 15)

4.10 ARE MOVING SUBARRAYS NECESSARY?

While the Geocoronal lines remain fixed on the detector with telescope slews, the target spectrum will shift in both DD and XD. The amount of spectral motion in pixels per arcsecond is given in Table 3. Multiplying these numbers by the aperture size (2.5”) and adding the PSF diameter (1.5”) gives the maximum possible spectral shift. These values are given in Table 4 in units of 6x25μm pixels, mm, and Å (DD).

Table 4: Maximum Spectral Shifts Due to Target Aperture Location

Grating	Max Dispersion Shift			Max Cross-Dispersion Shift	
	pixels	mm	Å	pixels	mm
G130M	180	1.1	1.7	38	0.9
G160M	180	1.1	2.0	43	1.0
G140L	188	1.1	11.2	41	1.0

Because many phases of TA rely upon absolute count rates, strong emission lines near the edges of fixed subarrays are a concern. For example, it is possible for a strong emission line to lie just outside of a fixed extraction subarray in one off-axis position, but be contained in the extraction subarray of another off- or on-axis position. In this case, it is possible for the off-axis counts to exceed those of a perfectly centered target. This scenario has called into question whether ``moving'' extraction subarrays are necessary. These moving extraction subarrays would shift in the dispersion direction based upon the aperture-detector mappings of Table 3.

Consider the case of a flat spectrum (flux =1 count per pixel), with a very strong narrow emission line (flux = 10,000 counts in one pixel) just outside the on-axis extraction subarray. Suppose that we are flux-centroiding in the dispersion direction using three dwells points of 1.2” offset with an initially on-axis pointing. The central (on-axis) dwell point will receive 10,000 counts for an extraction subarray with 10,000 pixels. An off-axis pointing of 1.2” places ~60% of the PSF in the aperture. Slewing in one direction will move the strong emission feature into the fixed extraction subarray giving this dwell point 0.6*(10,000 + 10,000) = 12,000 counts. The other direction will record 0.6*10,000 = 6,000 counts. In this case, the dispersion direction flux centroid would give a pointing error of 0.25”. In the less extreme case of a 1,000 count/pixel emission line the pointing error is 0.025”. **Therefore, in the vast majority of cases moving subarrays will not be required to achieve our TA accuracy goals.** Individual extreme cases can cause TA to exceed the TA accuracy goals with fixed subarrays.

4.11 EXTRACTION SUBARRAYS USED FOR TAACOS

Given the information of the previous sections, the choice of extraction subarrays is based solely upon the location and width of strong Geocoronal lines in the bandpass. Figure 18 below shows the TAACOS simulated G130M dispersion profile for daytime Geocoronal Lyα in wavelength and approximate DCS coordinates. The exact DCS to wavelength conversion will not be known until instrument I&T. The Geocoronal emission line fills the aperture and was assumed to be monochromatic (no Doppler width). HST/STIS/G140M spectra indicate that the Geocoronal Lyα Doppler width is less than 20 km s^{-1} (0.08Å). In TAACOS, we used extraction subarrays that excluded ±1mm around each of the features listed in Table 2. In addition, we excluded areas with 1mm of the detector active area edges. Given the image heights (±0.15mm for G130M and G160M; ±0.3mm for G140L), and the maximum detector shift due to location of the target in the aperture ~±1mm (Table 4), we used extraction subarrays of ±1.5 mm in the cross-dispersion direction for all gratings. These TAACOS TA extraction subarrays can be seen on the grating summary ``cheatsheets'' of COS-11-0017, and are listed explicitly in COS-01-0001 (OP-O1).

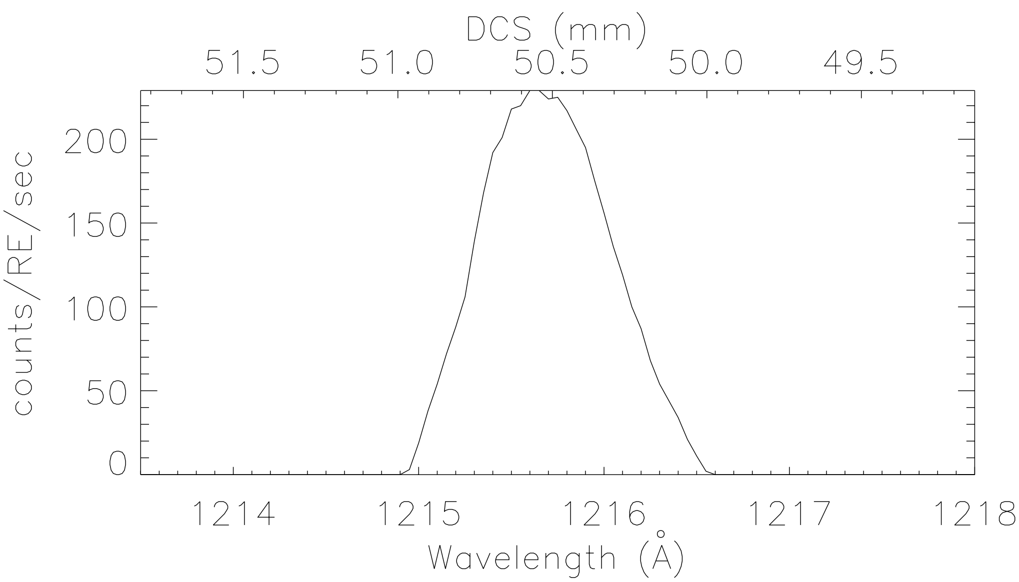

Figure 18: Dispersion profile of daytime G130M Geocoronal Lyα. Upper axis gives the approximate DCS coordinates corresponding to the given wavelengths. Left axis gives the predicted daytime Geocoronal countrate in units of counts per resolution element (RE) per second.

5. ANALYSIS BY TA PHASE

In this section, we examine each of the target acquisition phases described in the document OP-O1. For each phase, we will compare various options and scenarios to determine the efficiency and reliability of the TA phases. For each TA phase, we will also estimate the required execution time. We will report two estimates, one (in seconds(s)) will be our best approximation, and another (in minutes (m)) will be a conservation estimate produced by rounding our best estimates up to the next integer minute. The timing are for our $F_\lambda=10^{-15}$ ergs/cm^2/s/Å QSO source. Various assumption are made in producing the timing estimates:

1) The external shutter is closed at the beginning of TA, remains closed during LTACAL, and remains open during all other TA phases,
2) The detector voltage is ramped up from HVLOW to HVNOM at beginning of TA and remains at HVNOM for the duration of TA,
3) All HST slews less than 5" take 40s,
4) All HST slews, other than the initial pointing, are perfect (no pointing error), and
5) All TA phases and procedures are performed sequentially with no overlap.
6) Local count rate (BOP) exposures are performed for every exposure.

We designate the low voltage (down) state of the FUV detector as HVLOW and HVNOM as the nominal (up, high) voltage state for data collection. In addition, we abbreviate the cross-dispersion direction as XD, and the dispersion direction as DD. In our analysis we will be comparing initial HST pointings in the dispersion direction (DD, Y_0) and in the cross-dispersion direction (XD, X_0) to the final telescope pointings (Y_f and X_f). We will commonly compare the mean of the absolute value of the pointing errors. We designate this as $\langle|X_f-X_0|\rangle$ in the DD and $\langle|Y_f-Y_0|\rangle$ in the XD.

5.1 CALIBRATE APERTURE LOCATION (LTACAL)

5.1.1 Purpose

The calibrate aperture location procedure (LTACAL) locates the cross-dispersion spectral location of the Platinum-Neon (PtNe) calibration lamp on the detector. Photons from the calibration lamp follow a nearly identical optical path as those of a science observation, but are directed through a different aperture than science targets. The known offset between the calibration and science apertures allows one to determine the optimum location of the science target in the science aperture based upon the location of the calibration spectrum on the detector. Due to variations in the mechanical position of the grating and the conversion of photons into digitized pixels, it is expected that this procedure will be required for each target acquisition. This TA phase is performed before all other TA phases, and is performed with the external shutter closed.

5.1.2 Analysis

Figures 19-21 display example TAACOS calibration lamp spectra for the three FUV gratings. The upper panel shows the input Pt-Ne calibration lamp spectrum. Although these figures indicate an exposure time of 5s (S/N ~40), this is only a very crude estimate based upon preliminary calibration lamp fluxes. The actual exposure times are likely to be longer (~10s), but less than 30 seconds. The second panels of Figures 19-21 show the full and zoomed detector image. The third panel shows the extracted calibration spectrum, including instrument efficiencies, photon, and background noise. The bottom two figures show the XD profile of each FUV detector segment. Note the asymmetries in the XD profiles due to off-axis nature of the calibration spectra. Extraction subarrays of ±0.4mm are centered on the expected calibration XD location. For the TAACOS simulation, the XD range was ~2.1-2.9 in DCS Y coordinate. The full active area of the detector is used, except the G140L, where only segment A is used.

As outlined in COS-FSW-001, the expected algorithm is to use the mean XD position. However different algorithms may be required if the XD profile of the calibration lamp spectrum is not symmetrical or if the spectrum has a significant tilt with respect to IC rows and columns. The TAACOS simulations indicate that the spectrum does have a slight, but insignificant, tilt. We have tested the reliability of using the mean XD position against an algorithm that uses the median pixel location. We find that the difference between the median and mean is less than 0.3p (0.03” on the sky) for the medium resolution gratings and less than 0.45p (0.04”) for the G140L.

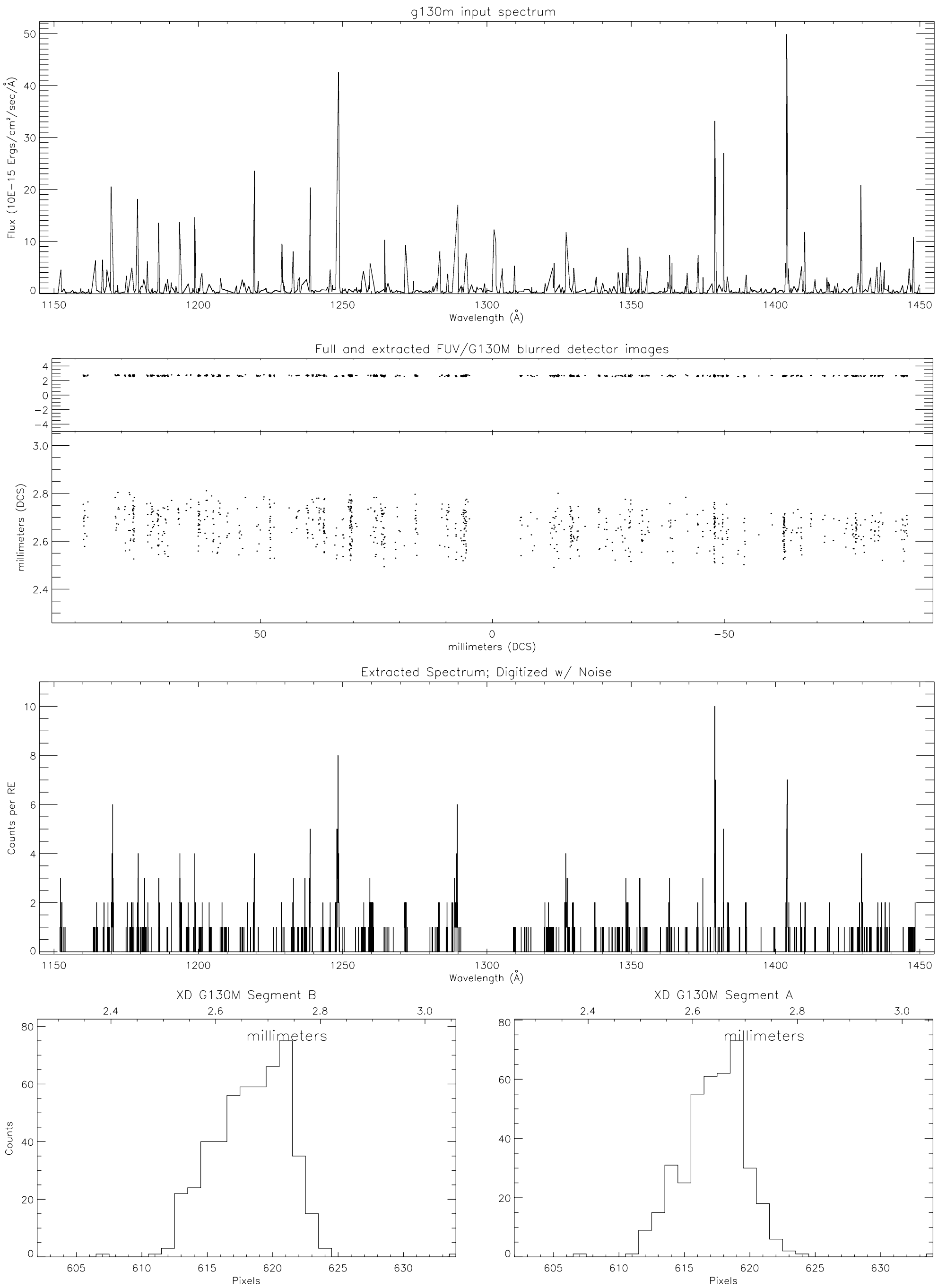

Figure 19: Pt-Ne wavelength calibration lamp G130M exposure. The upper panel shows the input Pt-Ne calibration lamp spectrum. The second panel shows the full and zoomed detector image. The third panel shows the extracted calibration spectrum. The bottom two figures show the cross-dispersion profile of each FUV detector segment.

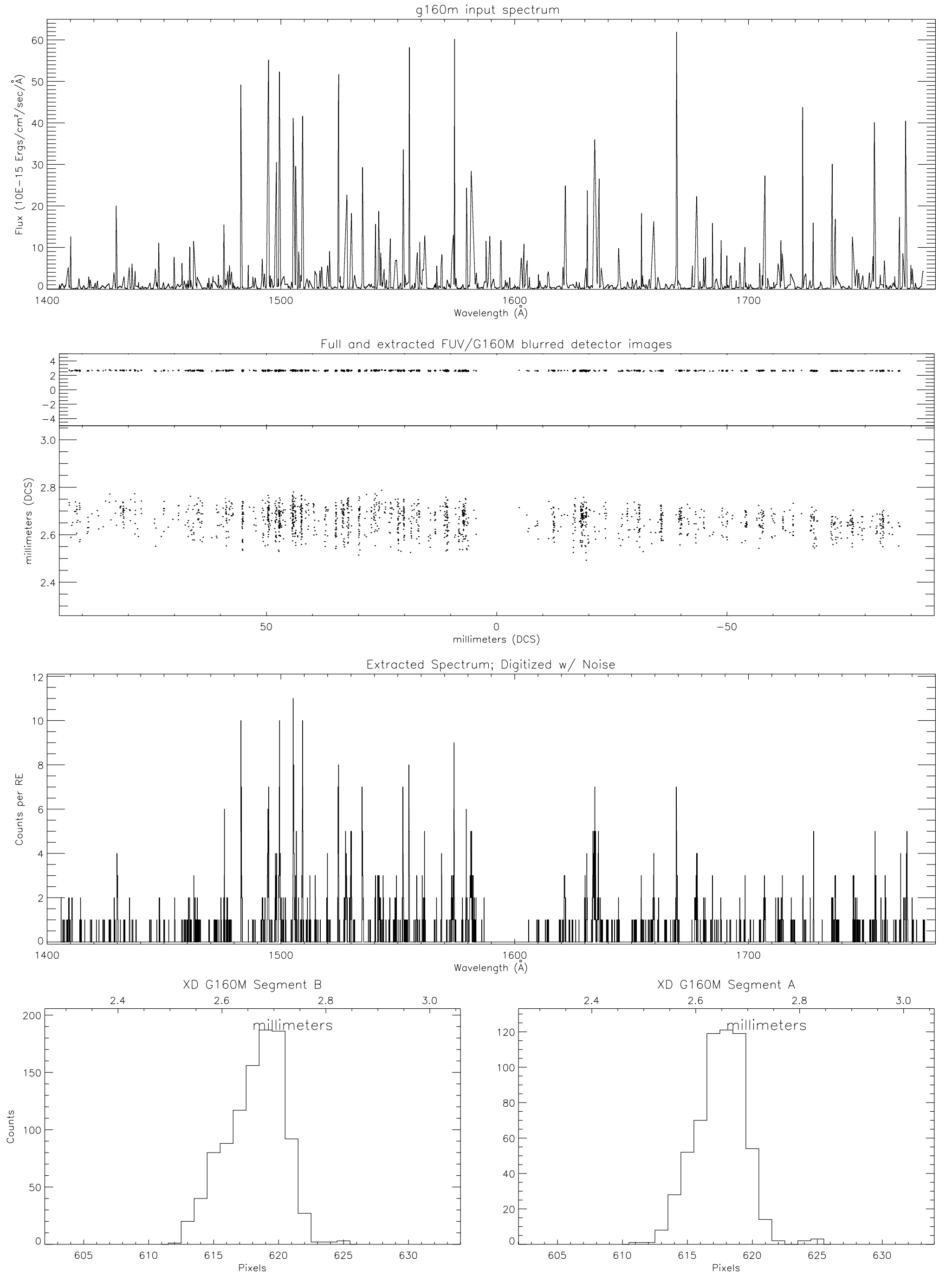

Figure 20: Pt-Ne wavelength calibration lamp G160M exposure. The upper panel shows the input Pt-Ne calibration lamp spectrum. The second panel shows the full and zoomed detector image. The third panel shows the extracted calibration spectrum. The bottom two figures show the cross-dispersion profile of each FUV detector segment.

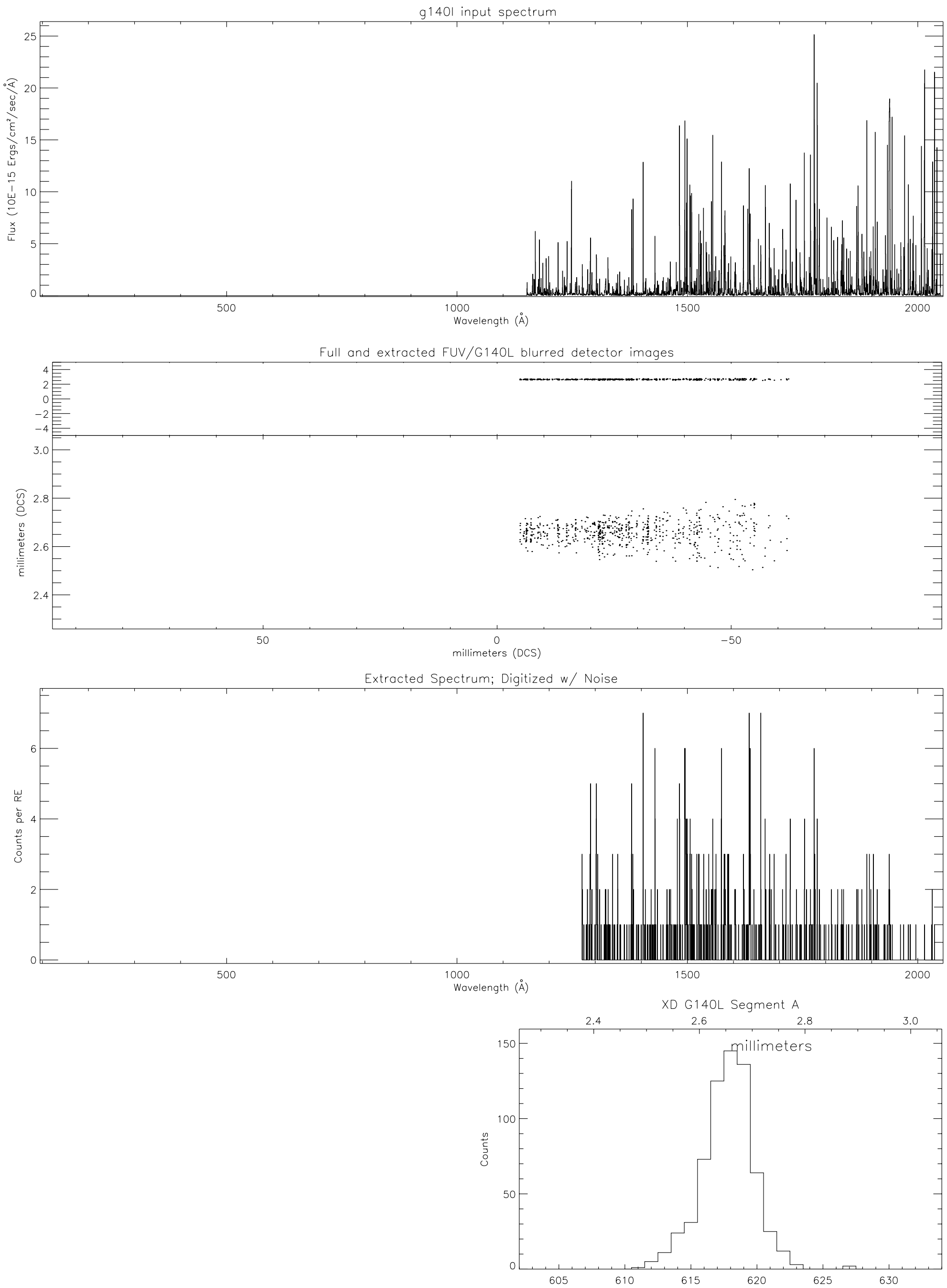

Figure 21: Pt-Ne wavelength calibration lamp G140L exposure. The upper panel shows the input Pt-Ne calibration lamp spectrum. The second panel shows the full and zoomed detector image. The third panel shows the extracted calibration spectrum. The bottom two figures show the cross-dispersion profile of each FUV detector segment.

5.1.3 LTACAL Timing

We assume the TA timing begins with LTACAL, after HST has acquired the guide stars and slewed to the approximate position requested by the observer. Assuming that the shutter is closed, and the detector is in a low voltage state (HVLOW) we estimate the LTACAL total time by:

TA FSW initialization	2s
High Voltage Ramp up	
(HVLOW >> HVNOM)	5s
Calibration Lamp Warmup	30s
BOP Check	10s
Calibration Lamp Exposure	10s
LTACAL software execution/overhead	5s
LTACAL TOTAL	62s

HVNOM is the nominal (high) voltage state for FUV detector data collection. BOP is the bright object protection check.

5.1.4 LTACAL Conclusions

Despite the obvious asymmetry in the cross-dispersion profile, if the proper subarrays are used, the mean and median cross-dispersion pixel values are always within one 25µm pixel (this equates to < 0.08" on the sky). Both detector segments were used for the G130M and G160M gratings, while only the longer wavelength segment of the G140L was used. Failure to use subarrays causes the mean cross-dispersion value to vary widely with background noise. A few photons far from the spectrum can pull the mean cross-dispersion coordinate off the calibration spectrum. Using the median cross-dispersion value does not require subarraying, but is much more computationally expensive. For the remainder of TAACOS, we use the mean cross-dispersion method with subarrays that extract ±0.4mm around the nominal cross-dispersion location of the calibration lamp. These extraction subarrays can be seen on the TA summary "cheatsheets" of COS-11-0017, and are listed explicity in COS-01-0001 (OP-01). LTACAL should be complete in 62s (or 2m in our conservative estimate).

5.2 TARGET SEARCH (LTASRCH)

5.2.1 Purpose

The spiral Target Search (TS) procedure (LTASRCH) is used to place the science target in the science aperture. Given the initial HST centering accuracy, and the 1.25” radius PSA/BOA, there is no guarantee that the target will be in the aperture after the initial HST pointing. The spiral TS pattern is specified by the number of dwell points, the offset distance between each dwell point, and the exposure time per dwell point. The mandatory TS centering accuracy is determined by requiring that the target spectrum is on the detector and is within some known detector subarray appropriate for the subsequent cross-dispersion peakup subarray (LTAPKXD) and dispersion peakup (LTAPKD) TA phases. Simply ensuring that the center of the target PSF is in the aperture satisfies this requirement. Three different center methods will be tested:

1) Return To the Brightest dwell point (RTB),
2) Return to the Flux Centroid of the dwell points (FC), and
3) Return to the threshold “Floored” Flux Centroid (FFC)

The extraction subarrays recommended in section 4.11 are used during LTASRCH to exclude strong Geocoronal emission lines.

5.2.2 Analysis

We find that for the medium resolution gratings, our $F_\lambda=10^{-15}$ ergs/cm^2/s/Å input spectrum achieves a S/N of 40 in 30 seconds using both detector segments. We use this exposure time for each dwell point in the spiral search. The G140L exposures achieve this S/N in 20 seconds using only segment `A’. With TAACOS, we have explored the TS parameter space in terms of the number of dwell points and dwell point offsets. We constructed simulations that compare spiral searches of 3, 4, and 5 dwell points on a side with varying offsets over the range of 0.75-2.3”. Figure 22 visually compares these spiral searches. Use of even number TS spiral searches requires that HST slew to a location other than the observer coordinates. This involves a change to the FSW, or that a new TA routine that slews an arbitrary offset be developed.

For our simulations, it is assumed that the initial HST pointing centers the target with a 1σ accuracy of 1". This is consistent with GHRS, FOS, and STIS acquisition histories. The majority of this error is observer error, and is not due to HST’s inability to slew to the proper sky location. It is not expected that TS will be 100% successful, as no TS can recover from errant target coordinates. However, given that COS may be observing the faintest targets ever observed with HST, and therefore the target coordinates may not be well known[3], we should expect to properly center on 3σ (initial slew off by 3"), and preferably 4σ cases. Our simulations for the different number of dwell points and dwell offsets were all tested against the same 1σ =1" random distribution of coordinate errors, so the results for each trial are directly comparable. The 3σ =3" area is indicated by the red circle in Figure 22. Our sample was forced to 3% of the trials outside the 3σ circle.

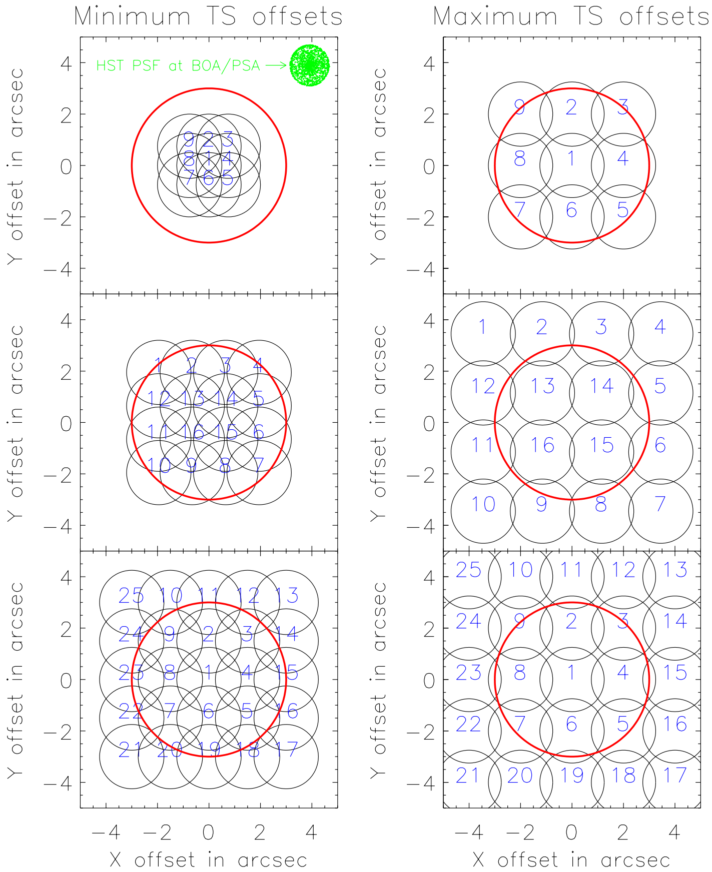

Figure 22: Sky location extents of the LTASRCH analysis. Upper left panel shows the 3x3x1.50" TS search pattern for the 2.5" diameter circular PSA. The HST PSF at the BOA/PSA is shown in green. The red circle indicates the 3σ=3" extent of the initial HST pointing error. Upper right panel shows the 3x3x2" offsets. Middle panels indicate the TS patterns for 4x4 grids with dwell point offsets of 1.3" (left) and 2.3" (right). Bottom panels indicate the TS pattern for 5x5 grids with offsets of 1.5" (left) and 2" (right). Dwell point counters are given in blue. These offsets correspond to the smallest, middle, and largest dwell point offsets indicated Table 5.

[3] The contrary may actually be true do to the availability of the GSC II catalog and other sky surveys. If this is actually the case, the TA strategies should be optimized for a smaller radius search.

Table 5 gives the results for the TS simulations, for both a return to brightest (RTB) and flux centroiding (FC) strategy. Our flux-centroiding algorithm only considers dwell points with a minimum number of counts (10) that are greater than 10% of the brightest dwell point. Given that the HST PSF is smaller in radius than the COS science apertures by 0.5" on the sky, shown in green in Figure 22, it is possible for a few (1-4) dwell locations to contain target photons depending on dwell point offsets. Use of a "floored" flux-centroid (FFC) will reduce this number by one, causing asymmetries in the flux-centroiding that produces poorer results. The FFC or threshold flux-centroiding algorithm is used for STIS TSs, and has been proposed to be used with COS. Results of our TAACOS suggest not using a FFC for any TS. As Table5, the RTB algorithm always produces results much worse than the FC algorithm. Table 5 also gives the worst cases (WC) for each of the 50 target acquisitions trials. For TS patterns without holes, the LTASRCH worst cases are dominated by the initial pointing offsets that lie outside the centers of the edge TS dwell points. These points also drive the reported standard deviations of the mean acquisition errors

Given the relationship between the HST PSF and the science apertures:

1) TS dwell point offsets greater than 1.767" allow portions of the sky/PSF to be unsampled during TS (holes open in the TS pattern).
2) TS dwell point offsets greater than 2" allow for the undesirable possibility of only one dwell point containing counts from the target.
3) TS dwell point offsets greater than 2.8" allow for the entire PSF to fall into a TS pattern.

Each of these conditions results in systematic error in the FC TS calculation for large offsets. However, small LTASRCH offsets require a larger number of LTASRCH dwell points to cover the same area. As the FC algorithm is interpolative, the FC returned by LTASRCH cannot be outside the center of the dwell points on the outer edge of the search pattern. For example, a 3x3 TS pattern with 2" dwell point offsets can only properly center targets offset by less than 2" (2σ) in the dispersion (DD) and cross-dispersion (XD) direction, or 2.8" on the diagonal. A 4x4 TS with 2" dwell point offsets can acquire 3" DD and XD initial pointing offsets (4.2" on the diagonal), while 5x5 searches with the same offset can acquire 4" DD and XD offsets (5.6" on the diagonal). Subsequent single TA phases can expand these areas by as much as 1.25" in DD and XD.

TAACOS simulations indicate that TS can routinely center point sources to within ±0.3" in both XD and DD, placing it within the previously described subarrays. In many cases, accuracies of ±0.2" in DD and ±0.1" in XD are achieved with LTASRCH. These cases are shown in red in Table 5. There appears to be a large "sweet spot" in regards to dwell point offset, which always includes the 1.767" offset which is the largest offset with continuous sky coverage. The LTASRCH patterns for 1.767" offsets are shown versus the HST PSF in Figure 23. For dwell points offsets near 1.767", essentially 100% of targets within the edge centers are acquired with 0.1" in both XD and DD (this will be shown later in Figure 25).

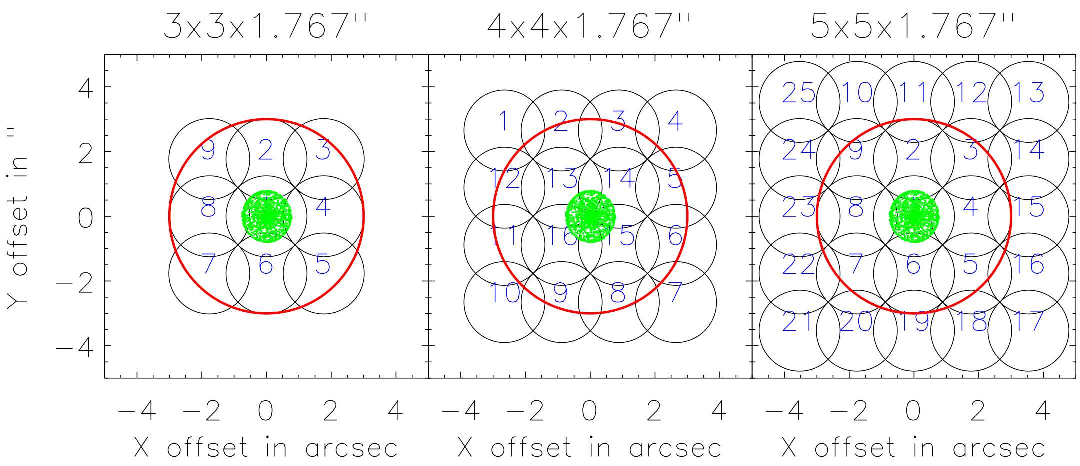

Figure 23: LTASRCH 1.767" search patterns compared to the HST PSF at the COS science apertures. The on-axis PSF is shown in green. The left panel shows the 3x3x1.767" search pattern with dwell point numbers given in blue. The middle and right panels show the 4x4 and 5x5 search patterns for 1.767" dwell point offsets. The red circle indicates the 3σ (3") search area.

As a further test of the robustness of the various LTASRCH number and offset of dwell point combinations, we compared the 3x3, 4x4, and 5x5 search patterns versus a circularly symmetric radial grid pattern of initial pointing error locations. The TAACOS radial search pattern test of LTASRCH is shown in Figure 24. This figure also shows the 4x4x1.767" TS in blue, and the HST PSF at the BOA/PSA in green. The PSF is positioned for one of the extreme radial test points. Since this point lies outside the TS search pattern, LTASRCH will fail for this TA. The 3σ (3") search area is also indicated by the red circle. In the case indicated in Figure 24, all LTASRCH locations would receive approximately the same airglow flux (if airglow occurs in the waveband, but not masked by the extraction subarrays), or zero counts. Both cases produce a LTASRCH FC that returns to the original HST pointing (the origin in Figure 24).

Table 5: TAACOS LTASRCH results

FUV	Search	Per TS	Step	# of	Return To Brightest Dwell Point				Return to (Threshold[a]) Flux Centroid			
Grating	Pattern	Offset	Time	Trials[b]	$<\|X_f - X_0\|>$	WC_X^c	$<\|Y_f - Y_0\|>$	WC_Y	$<\|X_f - X_0\|>$	WC_X	$<\|Y_f - Y_0\|>$	WC_Y
g130m	5x5	0.750"	30s	50	0.30±0.54"	3.68"	0.22±0.22"	1.30"	0.20±0.57"	3.68"	0.12±0.25"	1.30"
g130m	5x5	1.000"	30s	50	0.28±0.28"	1.68"	0.20±0.13"	0.46"	0.09±0.29"	1.68"	0.04±0.10"	0.59"
g130m	5x5	1.250"	30s	50	0.31±0.22"	1.18"	0.24±0.15"	0.59"	0.06±0.19"	1.18"	0.02±0.04"	0.25"
g130m	5x5	1.500"	30s	50	0.32±0.21"	0.76"	0.27±0.20"	0.67"	0.05±0.10"	0.68"	0.03±0.02"	0.10"
g130m	5x5	1.750"	30s	50	0.34±0.23"	0.86"	0.31±0.26"	0.85"	0.03±0.04"	0.27"	0.02±0.02"	0.06"
g130m	5x5	2.000"	30s	50	0.39±0.28"	0.97"	0.32±0.28"	0.95"	0.07±0.05"	0.20"	0.07±0.06"	0.24"
g130m	4x4	1.300"	30s	50	0.41±0.29"	1.73"	0.40±0.16"	0.65"	0.09±0.29"	1.73"	0.04±0.08"	0.45"
g130m	4x4	1.500"	30s	50	0.47±0.25"	1.43"	0.48±0.20"	0.72"	0.08±0.23"	1.43"	0.04±0.05"	0.34"
g130m	4x4	1.700"	30s	50	0.53±0.24"	1.13"	0.55±0.25"	0.83"	0.06±0.18"	1.13"	0.03±0.02"	0.13"
g130m	4x4	1.900"	30s	50	0.59±0.27"	0.97"	0.63±0.28"	0.92"	0.08±0.12"	0.83"	0.05±0.03"	0.12"
g130m	4x4	2.100"	30s	50	0.64±0.30"	1.05"	0.72±0.28"	1.02"	0.13±0.09"	0.53"	0.12±0.07"	0.28"
g130m	4x4	2.300"	30s	50	0.71±0.33"	1.15"	0.81±0.30"	1.12"	0.23±0.14"	0.56"	0.21±0.11"	0.45"
g130m	3x3	1.500"	30s	50	0.41±0.55"	3.68"	0.30±0.25"	1.30"	0.16±0.56"	3.68"	0.10±0.23"	1.30"
g130m	3x3	1.600"	30s	50	0.42±0.55"	3.68"	0.31±0.27"	1.30"	0.15±0.56"	3.68"	0.08±0.22"	1.30"
g130m	3x3	1.700"	30s	50	0.39±0.36"	1.98"	0.30±0.25"	0.84"	0.11±0.34"	1.98"	0.06±0.12"	0.70"
g130m	3x3	1.800"	30s	50	0.40±0.35"	1.88"	0.31±0.27"	0.91"	0.10±0.32"	1.88"	0.05±0.11"	0.60"
g130m	3x3	1.900"	30s	50	0.41±0.35"	1.78"	0.32±0.28"	0.95"	0.10±0.30"	1.78"	0.06±0.11"	0.60"
g130m	3x3	2.000"	30s	50	0.42±0.35"	1.68"	0.32±0.28"	0.95"	0.12±0.28"	1.68"	0.09±0.11"	0.70"
g160m	5x5	0.750"	30s	50	0.31±0.54"	3.68"	0.22±0.21"	1.30"	0.20±0.57"	3.68"	0.12±0.25"	1.30"
g160m	5x5	1.000"	30s	50	0.28±0.28"	1.68"	0.20±0.13"	0.46"	0.09±0.29"	1.68"	0.05±0.10"	0.60"
g160m	5x5	1.250"	30s	50	0.31±0.22"	1.18"	0.24±0.15"	0.59"	0.06±0.20"	1.18"	0.02±0.04"	0.26"
g160m	5x5	1.500"	30s	50	0.32±0.21"	0.74"	0.27±0.20"	0.67"	0.06±0.11"	0.68"	0.03±0.02"	0.10"
g160m	5x5	1.750"	30s	50	0.34±0.23"	0.86"	0.31±0.26"	0.85"	0.04±0.04"	0.29"	0.03±0.02"	0.08"
g160m	5x5	2.000"	30s	50	0.39±0.28"	0.97"	0.32±0.28"	0.95"	0.06±0.05"	0.17"	0.07±0.05"	0.17"
g160m	4x4	1.300"	30s	50	0.41±0.29"	1.73"	0.40±0.16"	0.65"	0.09±0.29"	1.73"	0.05±0.08"	0.45"
g160m	4x4	1.500"	30s	50	0.47±0.25"	1.43"	0.48±0.20"	0.72"	0.08±0.23"	1.43"	0.05±0.05"	0.33"
g160m	4x4	1.700"	30s	50	0.53±0.24"	1.13"	0.55±0.25"	0.83"	0.07±0.18"	1.13"	0.03±0.03"	0.13"
g160m	4x4	1.900"	30s	50	0.58±0.27"	0.95"	0.63±0.28"	0.92"	0.07±0.12"	0.83"	0.05±0.03"	0.12"
g160m	4x4	2.100"	30s	50	0.64±0.30"	1.05"	0.72±0.28"	1.02"	0.12±0.09"	0.53"	0.11±0.07"	0.26"
g160m	4x4	2.300"	30s	50	0.71±0.33"	1.15"	0.81±0.30"	1.12"	0.21±0.13"	0.56"	0.19±0.11"	0.41"
g160m	3x3	1.500"	30s	50	0.41±0.55"	3.68"	0.30±0.25"	1.30"	0.17±0.56"	3.68"	0.10±0.23"	1.30"
g160m	3x3	1.600"	30s	50	0.42±0.55"	3.68"	0.31±0.27"	1.30"	0.16±0.56"	3.68"	0.09±0.22"	1.30"
g160m	3x3	1.700"	30s	50	0.39±0.36"	1.98"	0.30±0.25"	0.84"	0.11±0.34"	1.98"	0.07±0.12"	0.70"
g160m	3x3	1.800"	30s	50	0.40±0.35"	1.88"	0.31±0.27"	0.90"	0.10±0.32"	1.88"	0.05±0.11"	0.60"
g160m	3x3	1.900"	30s	50	0.41±0.35"	1.78"	0.32±0.28"	0.95"	0.10±0.30"	1.78"	0.06±0.11"	0.60"
g160m	3x3	2.000"	30s	50	0.42±0.35"	1.68"	0.32±0.28"	0.95"	0.12±0.28"	1.68"	0.09±0.11"	0.70"
g140l	5x5	0.750"	15s	50	0.31±0.54"	3.68"	0.22±0.22"	1.30"	0.20±0.57"	3.68"	0.12±0.25"	1.30"
g140l	5x5	1.000"	15s	50	0.28±0.28"	1.68"	0.20±0.13"	0.46"	0.09±0.29"	1.68"	0.05±0.10"	0.60"
g140l	5x5	1.250"	15s	50	0.31±0.22"	1.18"	0.24±0.15"	0.59"	0.06±0.20"	1.18"	0.02±0.03"	0.23"
g140l	5x5	1.500"	15s	50	0.32±0.21"	0.76"	0.27±0.20"	0.67"	0.06±0.11"	0.68"	0.04±0.02"	0.10"
g140l	5x5	1.750"	15s	50	0.34±0.24"	0.89"	0.31±0.26"	0.85"	0.04±0.05"	0.30"	0.03±0.02"	0.10"
g140l	5x5	2.000"	15s	50	0.39±0.28"	0.97"	0.32±0.28"	0.95"	0.07±0.05"	0.20"	0.08±0.04"	0.17"
g140l	4x4	1.300"	15s	50	0.41±0.29"	1.73"	0.41±0.16"	0.68"	0.09±0.29"	1.73"	0.04±0.08"	0.45"
g140l	4x4	1.500"	15s	50	0.47±0.25"	1.43"	0.48±0.20"	0.72"	0.09±0.23"	1.43"	0.05±0.05"	0.34"
g140l	4x4	1.700"	15s	50	0.53±0.24"	1.13"	0.55±0.25"	0.87"	0.07±0.18"	1.13"	0.03±0.03"	0.20"
g140l	4x4	1.900"	15s	50	0.58±0.27"	0.95"	0.63±0.28"	0.98"	0.07±0.12"	0.83"	0.05±0.03"	0.11"
g140l	4x4	2.100"	15s	50	0.64±0.30"	1.07"	0.72±0.28"	1.02"	0.12±0.09"	0.53"	0.11±0.06"	0.24"
g140l	4x4	2.300"	15s	50	0.71±0.33"	1.16"	0.81±0.30"	1.18"	0.21±0.13"	0.56"	0.20±0.11"	0.43"
g140l	3x3	1.500"	15s	50	0.41±0.55"	3.68"	0.30±0.25"	1.30"	0.17±0.56"	3.68"	0.10±0.23"	1.30"
g140l	3x3	1.600"	15s	50	0.42±0.55"	3.68"	0.31±0.27"	1.30"	0.16±0.56"	3.68"	0.09±0.22"	1.30"
g140l	3x3	1.700"	15s	50	0.39±0.36"	1.98"	0.30±0.25"	0.84"	0.12±0.34"	1.98"	0.07±0.12"	0.70"
g140l	3x3	1.800"	15s	50	0.40±0.35"	1.88"	0.31±0.27"	0.91"	0.11±0.32"	1.88"	0.06±0.11"	0.60"
g140l	3x3	1.900"	15s	50	0.41±0.35"	1.78"	0.32±0.28"	0.95"	0.10±0.30"	1.78"	0.07±0.11"	0.60"
g140l	3x3	2.000"	15s	50	0.42±0.35"	1.68"	0.32±0.28"	0.95"	0.11±0.28"	1.68"	0.09±0.11"	0.70"

NOTE: Target Search trials which achieve $<|X_f - X_0|> < 0.2$" and $<|Y_f - Y_0|> < 0.1$" are denoted in red.

[a] Only dwell points above a threshold, currently 2% of the maximum, are considered.
[b] Number of random initial pointings used to determine the mean and standard deviations of the pointing errors. Each setup uses the same set of random pointings.
[c] WC: Worst case (largest pointing error) in $<|X_f - X_0|>$ (WC_X) or $<|Y_f - Y_0|>$ (WC_Y). Because each setup uses the same random pointings, these numbers are directly comparable between setups.

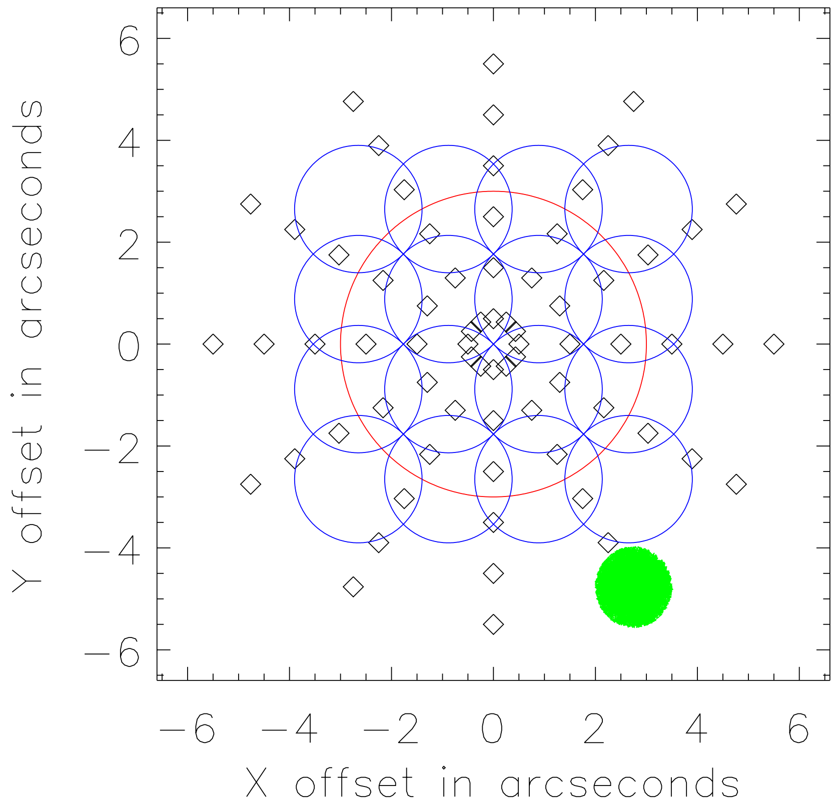

Figure 24: TAACOS radial search pattern test of LTASRCH. The 4x4x1.767" TS pattern is shown in blue. The HST PSF at the BOA/PSA is shown in green for one of the radial test points. Since this point is outside the TS search pattern, LTASRCH will fail for this TA. The 3σ (3") search area is indicated by the red circle. All TS locations would receive approximately the same airglow flux that lies outside the extraction subarrays, or no counts, producing a FC that returns to the original HST pointing.

The results of this test are shown in Figure 25. In this figure, the percentage of radial grid points recovered to within 0.1" in DD (top) and XD (bottom) is plotted versus grid point offset from the center of the aperture. Offsets near 1.75" are clearly superior to all other offsets tested. Note that the 2" LTASRCH offset creates holes in the TS area, and in some cases, only 1 TS dwell point receives target flux. This prevents the 2" offset LTASRCH from recovering target positions to within 0.1".

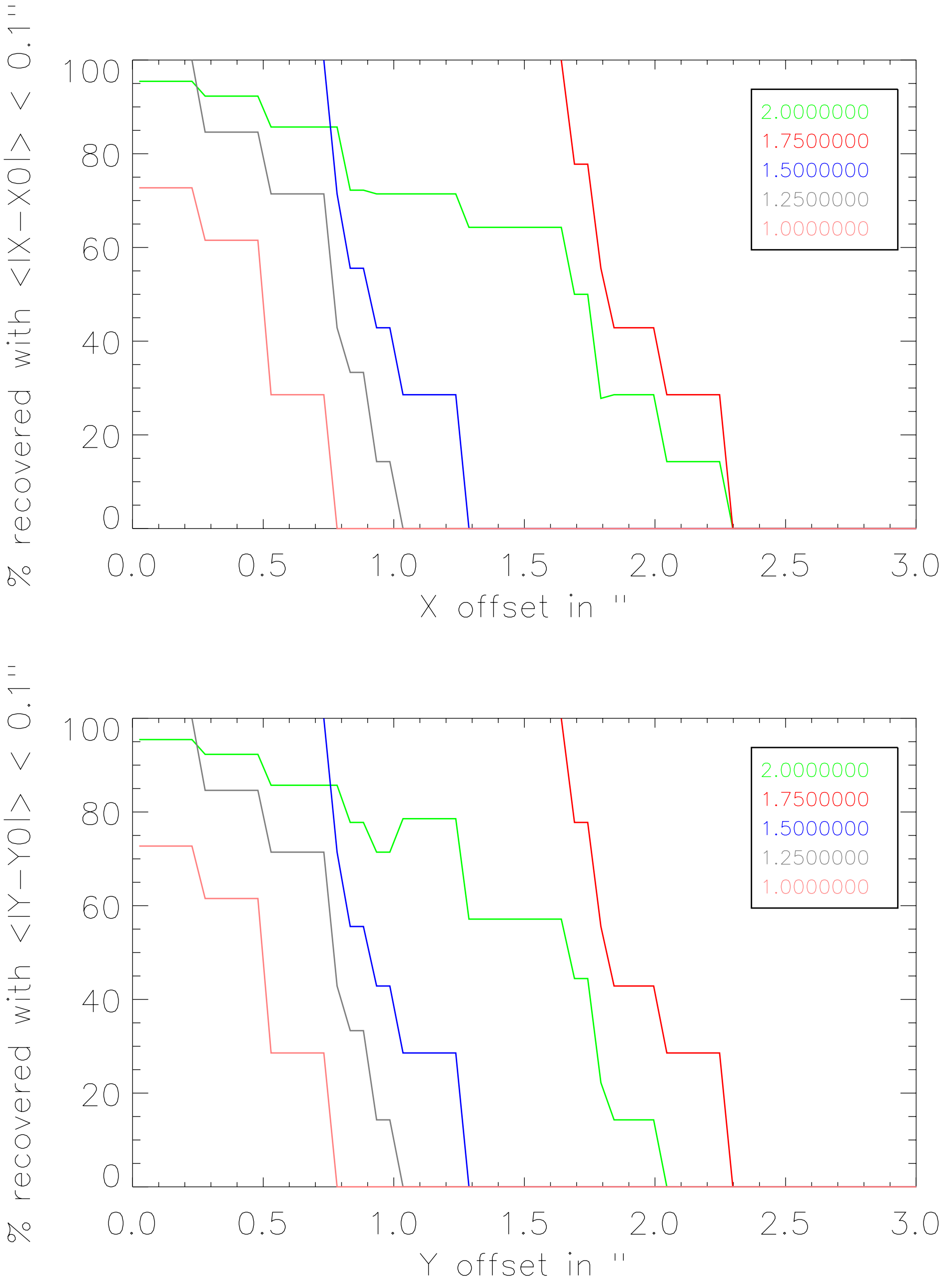

Figure 25: LTASRCH radial grid results for a 3x3 TS pattern. The left axis gives the percentage of radial grid points recovered to within 0.1" in DD (top) and XD (bottom). Of the LTASRCH offsets tested, 1.75" appears to be best LTASRCH option. Note that in the 2" offsets, some grid positions are not recovered due to holes in the TS pattern.

5.2.3 LTASRCH Timing

LTASRCH consists of a series of HST slews plus one additional slew after calculating the FC of the TS. For even numbered TSs (i.e. 4x4), one additional slew is required before initiating the spiral search, unless the current FSW routines are modified.

For each dwell point, the required time is:

BOP Check	10s
LTASRCH Exposure for a $F_{\lambda}=10^{-15}$ ergs/cm^2/s/Å source	30s (20s for G140L)
HST Slew to next location (or FC if last)	40s
LTASRCH each dwell point	80s (70s for G140L)

After the last dwell point:

LTASRCH FC calculation/overhead	5s
LTASRCH after last dwell point	5s

Table 6 gives the timing estimates for 2x2, 3x3, 4x4, and 5x5 searches as calculated (in seconds) or rounded up to the next minute for all FUV gratings. Before the LTASRCH phase, the external shutter must be commanded open from the ground.

Table 6: LTASRCH Duration Estimates

LTASRCH Pattern	Exposure Time (ET) Calculation for G130M/G160M (G140L)	ET as calculated (seconds)		ET rounded up (minutes)	
		G130M/ G160M	G140L	G130M/ G160M	G140L
2x2	80s (70s)*4 +40s +5s	365	325	7	6
3x3	80s (70s)*9 + 5s	725	635	13	11
4x4	80s (70s)*16 + 40s + 5s	1325	1165	23	20
5x5	80s (70s)*25 + 5s	2005	1755	34	30

5.2.4 LTASRCH Conclusions

There are an infinite number of dwell point number and offsets that will achieve the desired result of ensuring that the target is in the aperture, assuming that the TS extent is large enough to sample the PSF center. Targets outside the edge centers of the TS pattern can be centered to no better then the distance from the PSF center to the closest TS pattern dwell point. TS patterns which do not sample the PSF will, obviously, fail. This can happen if the number and offsets of the TS are too small, or if the offsets are so large (>2.8") that the entire PSF falls in a TS pattern hole. The offset of 1.767" is the offset at which diagonal dwell points just overlap (the largest offset without any holes). There appears to be a large offset "sweet spot" between 1-2" in which all TS patterns achieve offset errors of less than 0.2" in the DD and 0.1" in the XD direction. The errors always approach their minimum value near the 1.767" offset. Therefore, unless one wishes to increase the offset solely for the purpose of extending the search area, 1.767" consistently appears to be near the center of the LTASRCH offset "sweet spot" for all trials. LTASRCH offsets greater than 2" should be avoided. At this offset, and greater, it is possible for only one TS dwell point to sample the PSF, introducing error into the FC calculation. It should be noted that some of the LTASRCH trials listed Table 5 already approach, and some exceed, the TA acquisition goal of 0.1" (3σ) in both XD and DD.

Specifically, the 5x5x1.767" trial appears to meet the TA goals by itself, without the aid of the other TS phases. Furthermore, this pattern fully samples a 2x1.767" = 3.53σ initial error offset range. However, this phase takes ~31-35 minutes. As will be demonstrated in the following sections, performing the smaller 3x3 or 4x4 searches, followed by other TA routines can exceed the results of this trial in less time, while sampling the same area.

5.3 PEAKUP IN THE CROSS-DISPERSION DIRECTION (LTAPKXD)

5.3.1 Purpose

The peakup in the cross-dispersion direction (LTAPKXD) is intended to improve the centering of the science target in the direction perpendicular to the dispersion. If the LTASRCH phase was previously successfully executed, the target is ensured to be in the aperture. This guarantees that the target spectrum will be within a known subarray on the detector, but it may not be in the optimum cross-dispersion location. The LTAPKXD procedure will measure the cross-dispersion location of the spectrum and attempt to move the telescope to place the target in the center of the aperture in the cross-dispersion (XD) direction. The initial approximate location of the spectrum is known from the LTACAL phase. The same LTACAL algorithms for determining the cross-dispersion location of the LTACAL spectrum (mean and median) will be compared in locating the XD center of the target spectrum during the LTAPKXD testing. The extraction subarrays recommended in section 4.11 are used to exclude strong Geocoronal emission lines, which have a different XD profile than point sources. The XD pixel size was assumed to be 25μm.

5.3.2 Analysis

To test the LTAPKXD procedure, a 7x7x0.05” pointing error grid was used to simulate the HST pointing parameter space expected after a successful LTASRCH. This grid is shown in Figure 26. In this figure, the HST PSF is shown in green, the extent of the PSA/BOA in red, and the 7x7x0.05” grid is shown in blue. The input QSO spectrum is placed at each indicated position, then the LTAPKXD procedure is executed. For each grating, exposure times of 10s, 30s, 60s, 120s and 240s were measured to determine the mean and median XD coordinate. These results are summarized in Figure 27. In this figure, mean results are shown in green and median results are shown in red. Solid lines indicate the mean or median XD pointing errors after LTAPKXD. Standard deviations about the mean and median are also shown. The dashed lines indicate the 3σ XD pointing errors.

The off-axis and dispersion axis variance of the cross-dispersion profile affects the LTAPKXD procedure. The bimodal G130M XD profile requires more time to determine the mean than the symmetric XD profiles of the G160M and G140L. Off-axis, the relative strength of the G130M XD profile peaks changes drastically. However, as shown in Figures 15-17, there appears to be a linear relationship between off-axis position and cross-dispersion coordinate for all three FUV gratings.

As with the LTACAL procedure, the inclusion of extraction subarrays is essential when using the mean to calculate the XD position of the spectrum. As shown in Figure 27, using the median XD pixel location appears to be a slightly better indicator of the XD spectral center. However, the 3σ error for most of the mean and median LTAPKXD trials is less than 0.1”. For comparison, an offset of 0.1” in the XD direction equates approximatel one 25μm XD pixel.

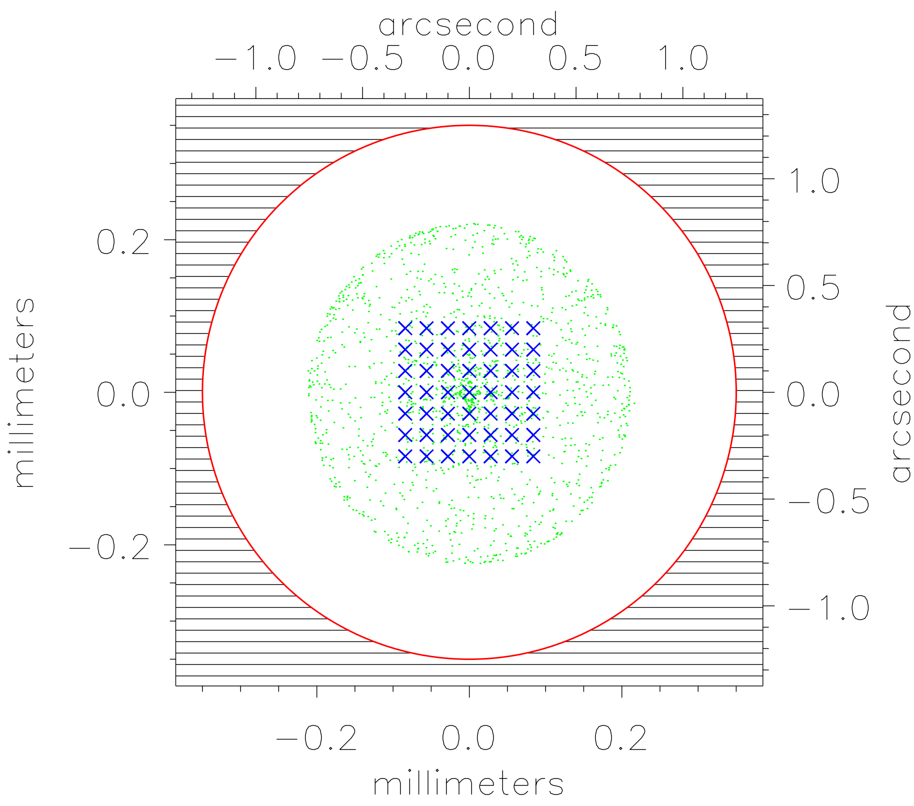

Figure 26: Test Grid for LTAPKXD. The COS PSA/BOA is indicated by the red circle. The HST PSF at the PSA/BOA is shown in green. The 7x7x0.05” test grid for LTAPKXD is shown in blue. A point source is placed at each position indicated, and the LTAPKXD routine is applied to the detected spectrum.

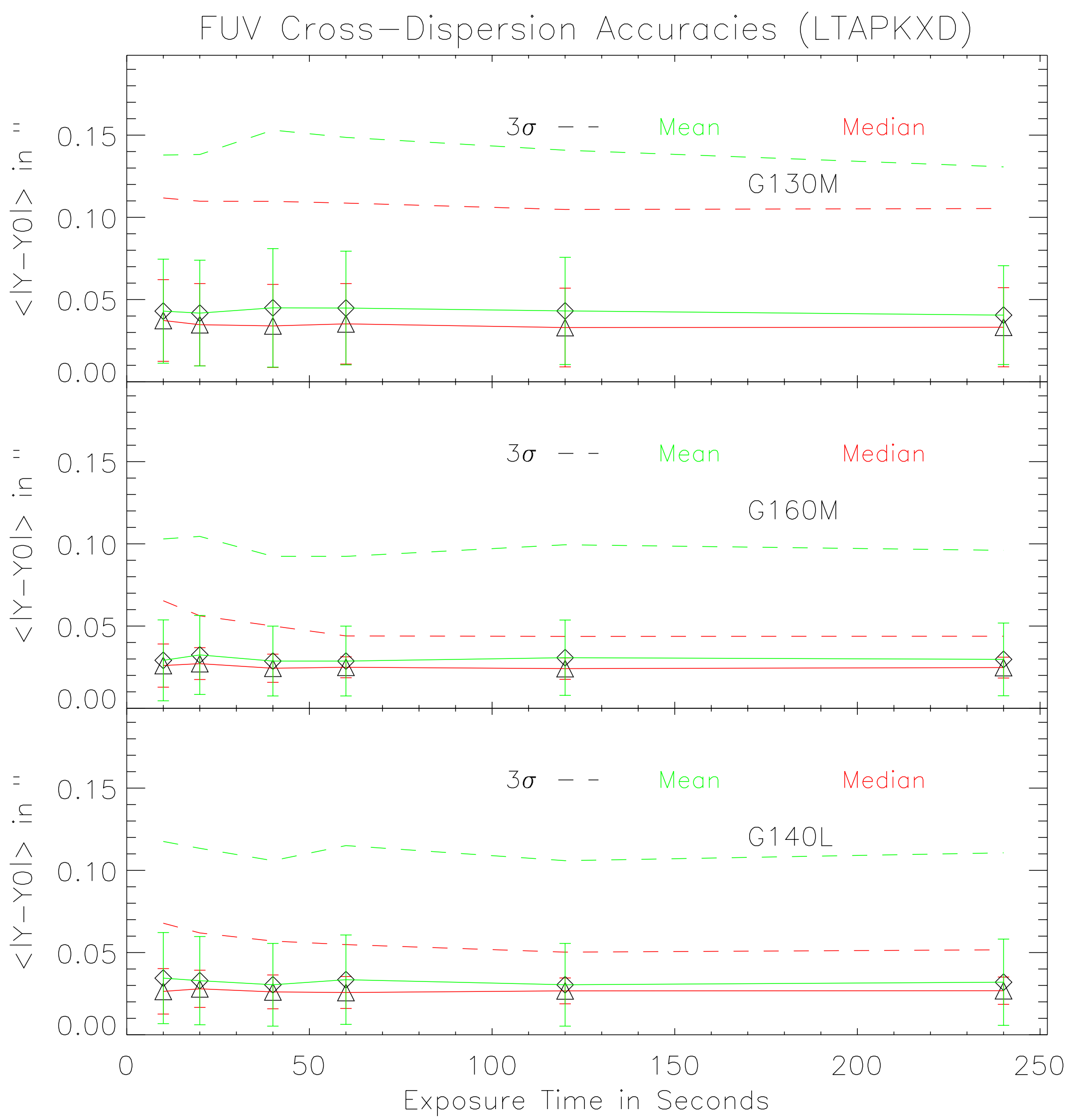

Figure 27: LTAPKXD TAACOS tests results. The XD recovery error (in arcseconds) is plotted versus exposure time of our input spectrum. XD coordinates recovered using a mean algorithm are shown in green, while the median results are shown in red. Dashed lines indicate the 3σ recovery boundaries. Note that due to the bimodal XD profile of the G130M spectrum, the LTAPKXD mean 3σ recovery boundary is higher than the other gratings. However, this recovery error is still much less than the 0.3" requirement.

5.3.3 LTAPKXD Timing

BOP Check	10s
LTAPKXD Exposure for a	
$F_\lambda=10^{-15}$ ergs/cm^2/s/Å source	30s for G160M
	60s for G130M
	20s for G140L
LTAPKXD software execution/overhead	2s
LTAPKXD slew	40s
LTAPKXD TOTAL	112s for G130M (3m)
	82s for G160M (2m)
	72s for G140L (2m)

5.3.4 LTAPKXD Conclusions

The LTAPKXD TA phase easily aligns targets to within 0.1” in the XD in the 3σ case for initial pointing offsets of up to 0.3” in both XD and DD. Using the median XD coordinate gives better accuracy than the mean algorithm, but is not sufficiently better to warrant recommending the addition of a FSW routine to calculate the median value. The bimodal cross-dispersion profile of the G130M implies that a longer integration time is necessary for this grating during LTAPKXD. It should be noted that the final XD TA accuracy is the combination of the LTACAL accuracy plus the calculated LTAPKXD offset. This TA phase should take 2-3 minutes for an $F_\lambda=10^{-15}$ ergs/cm^2/s/Å source, depending on grating.

5.4 PEAKUP IN THE DISPERSION DIRECTION (LTAPKD)

5.4.1 Purpose

The LTAPKD TA procedure is intended to improve the centering of the science target in the dispersion direction (DD). This TA phase is designed to maximize flux at the detector. This differs from the LTAPKXD phase that positions the spectrum on the detector. In LTAPKD, HST is moved through a series of DD dwell point. The number and sky separations of dwell points are TBD. In LTAPKD, only the total flux within a specified subarray is needed to determine the best telescope pointing. As with the LTASRCH procedure, the algorithms to be tested are:

1) Return to the brightest dwell point (RTB),
2) Return to the flux-weighted centroid (FC) of the dwell points, and
3) Return to the flux-weighted centroid with the lowest count dwell point excluded (a floored flux centroid, FFC).

The extraction subarrays recommended in section 4.11 are used to exclude strong Geocoronal emission lines.

5.4.2 Analysis

To test the LTAPKD TA phase, we used an identical 7x7x0.05" target offset grid used in the LTAPKXD testing (Figure 26). We tested LTAPKD for 3, 4, 5, 7, and 9 dwell points with maximum DD offsets of ±1.2". The setup for the 5x0.06" LTAPKD trial is shown in Figure 28. In this figure, the HST PSF is shown in green at the center of the search pattern, and the colored x's correspond to the aperture positions of the same color.

Figures 29-31 show the FC and FFC results of our simulations for the three FUV gratings. In all cases, FC and FFC results were superior to RTB centering (not shown in the figures). This is not surprising given the PSF and aperture dimensions, as more than one dwell point could contain the full PSF. For all gratings, the FFC results are better for dwell point numbers of five and higher. The best results were obtained for a FC using 3x1.2" offsets. FC's with higher number dwell points suffered from asymmetries in the FC pattern, skewing the final centering towards the middle of the pattern. The FFC algorithm partially alleviates this problem by eliminating the farthest removed dwell point from the FC calculation. FFC's with fewer than five dwell points introduced asymmetries into the pattern, reducing the LTAPKD centering accuracy. Larger LTAPKD pattern extents than ±1.2" (e.g. 5x1") did not produce better results than the 3x1.2" pattern.

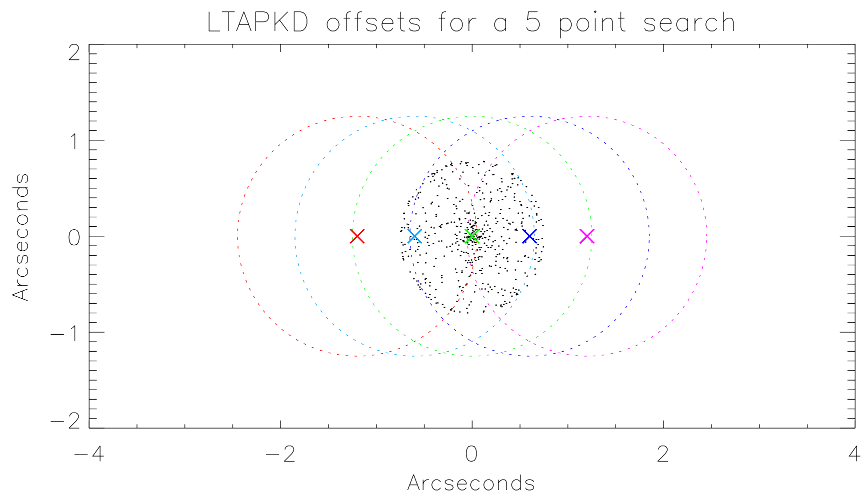

Figure 28: LTAPKD offsets for a 5x0.6" dwell point search. The colors of the aperture extents correspond to the dwell point center colors (x's). The HST PSF at the PSA/BOA is shown at the center dwell point location.

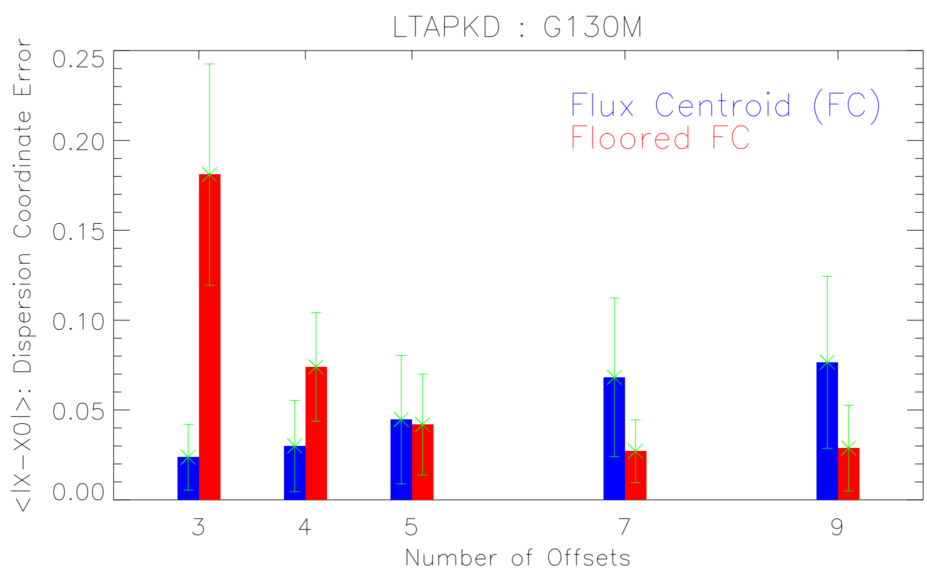

Figure 29: G130M LTAPKD test results. A 7x7x0.05" grid (Figure 26) was used to simulate target positions after performing a LTASRCH target search. Blue bars indicate the mean DD coordinate error after performing the LTAPKD procedure using a flux centroid (FC) algorithm to calculate the target location in the aperture. Standard deviations are indicated in green. Red bars give the results for a floored FC algorithm.

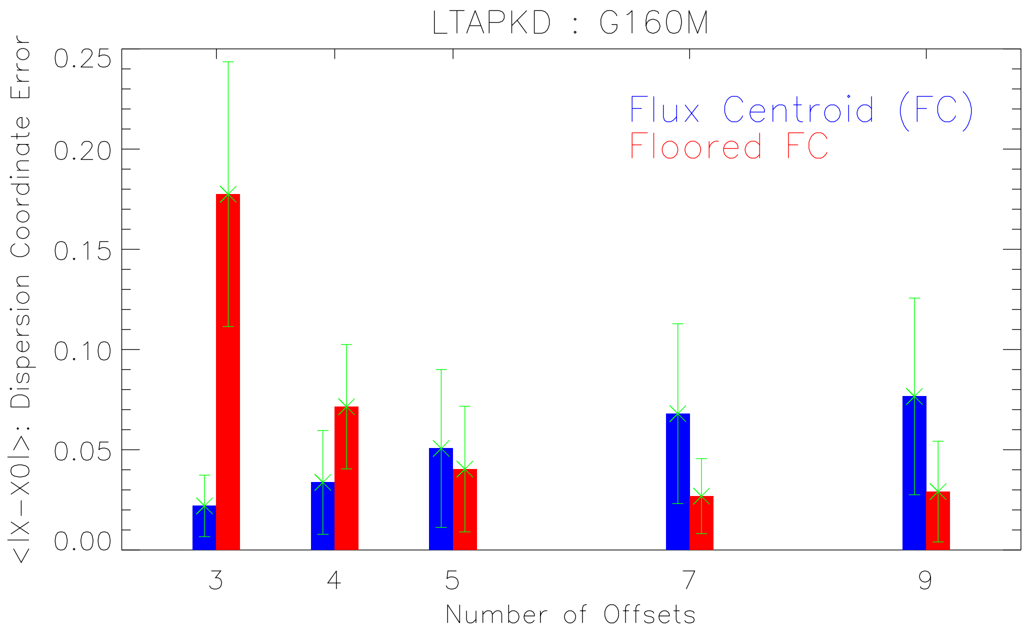

Figure 30: G160M LTAPKD test results. See Figure 29 for description.

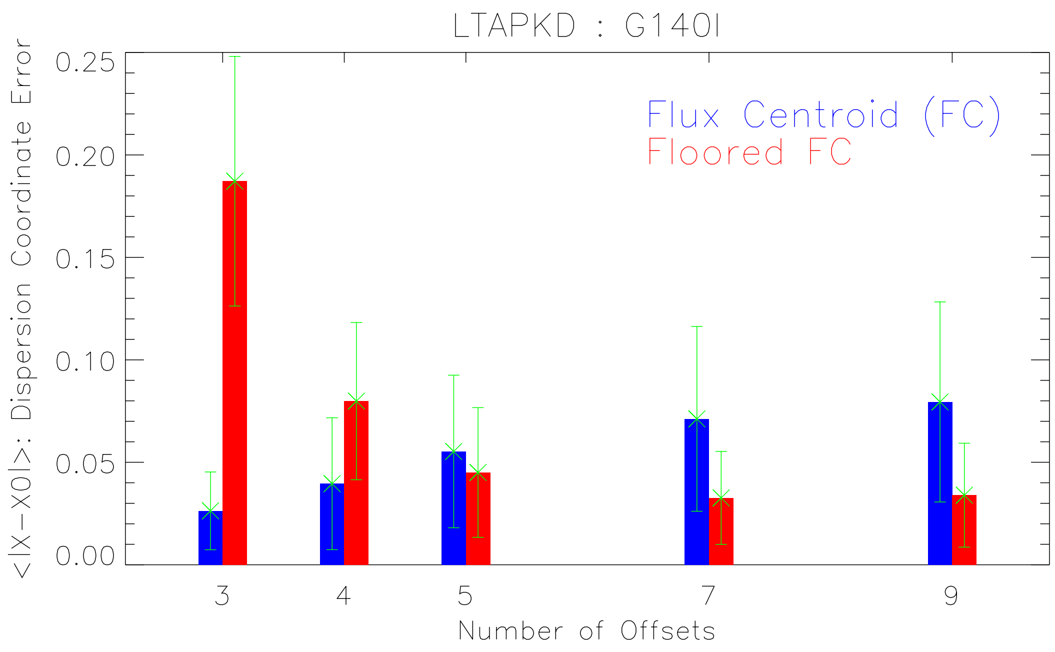

Figure 31: G140L LTAPKD test results. See Figure 29 for description.

5.4.3 LTAPKD Timing

Assuming that the external shutter is open, and the FUV detector is in the HVNOM state, each LTAPKD dwell point should take:

BOP Check	10s
LTAPKD Exposure	30s (20s for G140L)
LTAPKD slew	40s
Total	80s (70s for G140L)

In addition, we allot 5s for LTAPKD software execution/overhead. Therefore a three dwell point LTAPKD would take (3x80s)+5s = 245s (215s for G140L), or 5m (4m for the G140L) using our conservation round up to the next minute scheme.

5.4.4 LTAPKD Conclusions

Many LTAPKD patterns achieve the desired 0.1" centering accuracy. The flux centroid (FC) algorithms were superior to the return to brightest centering results. Floored FC results were better than FC results when five or more dwell points were used. The best LTAPKD centering accuracy is achieved using a 3x1.2" FC pattern. We estimate that this TA phase (with a three dwell point grid) will take 245s for the medium resolution gratings (215s for G140L), or 5m (4m for the G140L) using our conservative estimate. For our test grid, this produced mean DD centering accuracies ($<|X_F-X_0|>$) of 0.03". Accuracies and standard deviations using a FC 3x1.2" grid for each grating are given in Table 7 below.

Table 7: LTAPKD results for a 3x1.2" grid.

GRATING	$<\|X_F-X_0\|>$
G130M	0.018± 0.014 "
G160M	0.022±0.018"
G140L	0.029±0.025"

6. COMPARISION OF TA STRATEGIES

In this section, we will compare various TA strategies for a 3σ=3" initial pointing error distribution, and for a 3σ=1" distribution. Although historically, a 3σ=3" distribution is what we might for COS observers based upon past HST initial pointings, new digital sky catalogs such as the GSC II may enable COS observers to submit target coordinates more consistent with a 3σ=1" distribution. Additionally, some observers may know the coordinates of their targets at within 1" (e.g. the target has previously been observed with HST) or they may not need wavelength accuracies of 15 km/s (e.g. a QSO observer may wish to align the Galactic absorption features to the local standard of rest (LSR) as opposed to the heliocentric wavelength scale provided by HST). All comparisons are for our $F_\lambda=10^{-15}$ ergs/cm^2/s/Å QSO source, observed at S/N = 40.

6.1 COMPARISON OF TA STRATEGIES FOR A 3σ=3" DISTRIBUTION.

To compare the various TA strategies, we consolidated 250,000 possible TA scenarios down to eight strategies that appeared most promising from initial TAACOS simulations. These eight scenarios were tested against a population of initial pointing errors that was a combination of a 3σ=3" Gaussian distribution, plus a more uniform (4σ) component of approximately equal strength to build up number statistics at higher initial pointings errors. The DD distribution of initial target positions is shown in Figure 34. The eight scenarios tested were:

1) A 5x5x1.767" LTASRCH,
2) A 4x4x1.767" LTASRCH followed by a 2x2x1.767" LTASRCH,
3) A 3x3x1.767" LTASRCH followed by a 2x2x1.767" LTASRCH,
4) A 2x2x1.767" LTASRCH,
5) A 2x2x1.767" LTASRCH followed by a 2x2x1.767" LTASRCH,
6) A 3x3x1.767" LTASRCH followed by a LTAPKXD followed by a 5x0.6" LTAPKD (OP-O1-A),
7) A 3x3x1.767" LTASRCH followed by a LTAPKXD followed by a 3x1.2" LTAPKD (OP-O1-B), and
8) A 3x3x1.767" LTASRCH followed by a 3x1.2" LTAPKD followed by a LTAPKXD (OP-O1-C). This strategy is designed to test whether the order of the XD and DD TA phases was important.

The cumulative distribution results of these simulations are presented Figure 32. In this figure, the left axis gives the percentage of TA's which achieve $<|X_f-X_0|>$ (top, DD) and $<|Y_f-Y_0|>$ (bottom, XD) within the target search error indicated by the bottom axis in arcseconds. As before, X_f designates the final ACS pointing and X_0 the initial ACS target location in the dispersion direction (XD). Similarly, Y designates the cross dispersion direction (XD). These cumulative distributions are a good measure of the overall TA accuracies as measured by TAACOS. As shown in this figure, all of eight scenarios align the target in XD direction to within 0.1" greater than 95% of the time, except the 2x2x1.767" scenario. This is not surprising, since many of the initial pointings produce little or no counts in the 2x2 search. In the DD, the double spiral searches are better than the OP-O1 derivative scenarios in centering the target in the aperture. The inset plot gives the actual initial pointing distribution (X_0 vs. Y_0), and the 3σ (3") radius is shown in red.

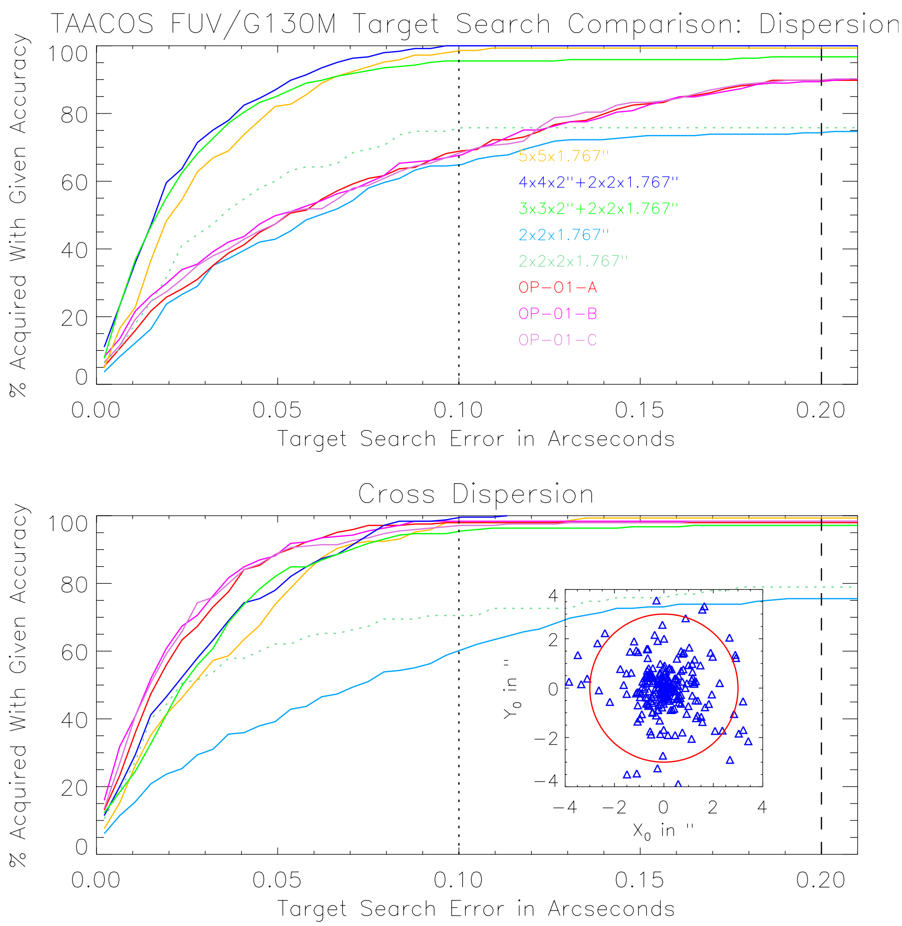

Figure 32: Comparison of TA strategies for a 3σ=3" distribution. TA's were simulated for an $F_\lambda=10^{-15}$ ergs/cm^2/s/Å QSO acquired with the G130M. Left axis gives the percentage of TA's which achieve $<|X_f-X_0|>$ (top, DD) and $<|Y_f-Y_0|>$ (bottom, XD) within the target search error indicated by the bottom axis in arcseconds. The sky distribution of initial target positions is shown in the inset plot. The 3σ=3" area is indicated by the red circle.

To test the spatial extent of the various TA strategies, Figure 36 plots the radial accuracy extents of the eight tested TA strategies for the 3σ=3” distribution. The bottom axis gives the initial pointing errors versus the recovery percentages within 0.1” for the DD (top), XD (middle) and radial dimension ($<|R_f-R_0|>$). The results are smoothed by a 1” moving boxcar filter. In some cases, the recovery rates are exactly the same (usually 100%), so some strategies are difficult to track in this figure. As expected, all TA strategies fall off in centering accuracy as the initial pointing error exceeds the offset where the HST PSF no longer yields any counts in the LTASRCH dwell point search pattern. Some anomalies in Figure 36 are due to initial point errors of large radial, but small DD or XD coordinate (the initial pointing error is small in one dimension, but large in the other). As shown in the previous figure, the OP-01 based searches rival the double spiral searches in the XD direction, but fail to achieve adequate TA accuracies in the dispersion and radial directions.

Overall TA accuracy must be balanced by total elapsed time to determine the best TA strategies. Since the DD centering accuracy is the important science driver, we focus on DD accuracy as a function of time for our eight TA scenarios. In Figure 35, we plot the percentage of target acquisitions that achieve a DD centering accuracy of < 0.1” versus the total elapsed time as predicted in the previous sections. The horizontal error bars represent the temporal extent for the three FUV gratings. The solid colored circles indicate the maximum expected TA time using our conservative (round up to the next minute at each phase) estimates. The vertical error bars are taken as the square root of the number of trials. The initial DD distribution is shown as the inset histogram of number (N) versus initial radial position (R_0). Only pointings with radial initial offsets with $R_0 <$ 3” were considered in this comparison. In this comparison, for this DD distribution, the best TA strategies appears to be the 3x3x1.767” +2x2x1.767” LTASRCH. If minimizing TA elapsed time is a priority over absolute assurance that the target is well centered, the 2x2x2x1.767” LTASRCHs is a viable alternative.

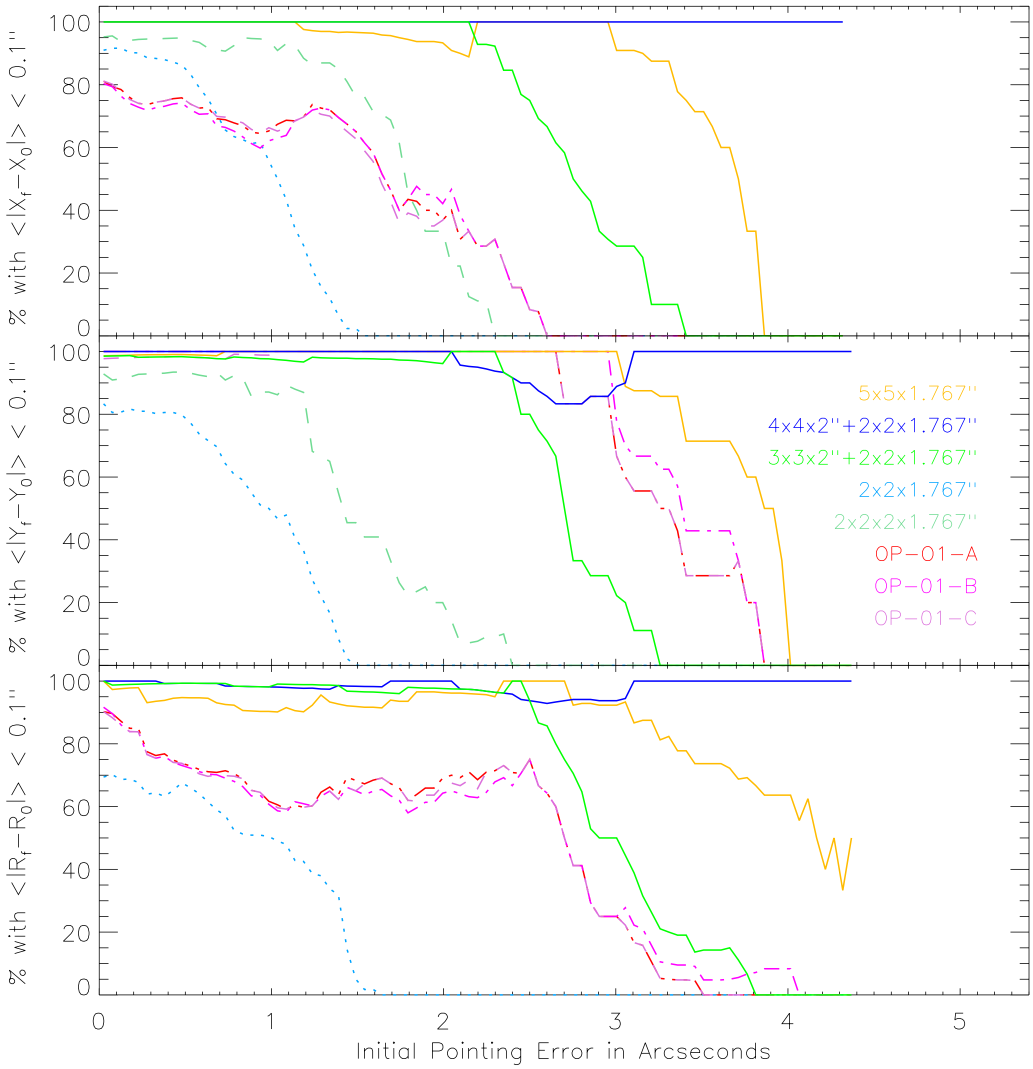

Figure 33: Radial accuracy extents of the TA strategies for a 3σ=3" distribution The left axis gives the percentage of targets acquired to within 0.1" for DD (top), XD (middle) and in radius (R, bottom). A one arcsecond moving box has been used to smooth the data. The DD and XD distribution of initial target positions (X_0 and Y_0) is shown in Figure 32, while the radial (R_0) distribution is shown in Figure 34.

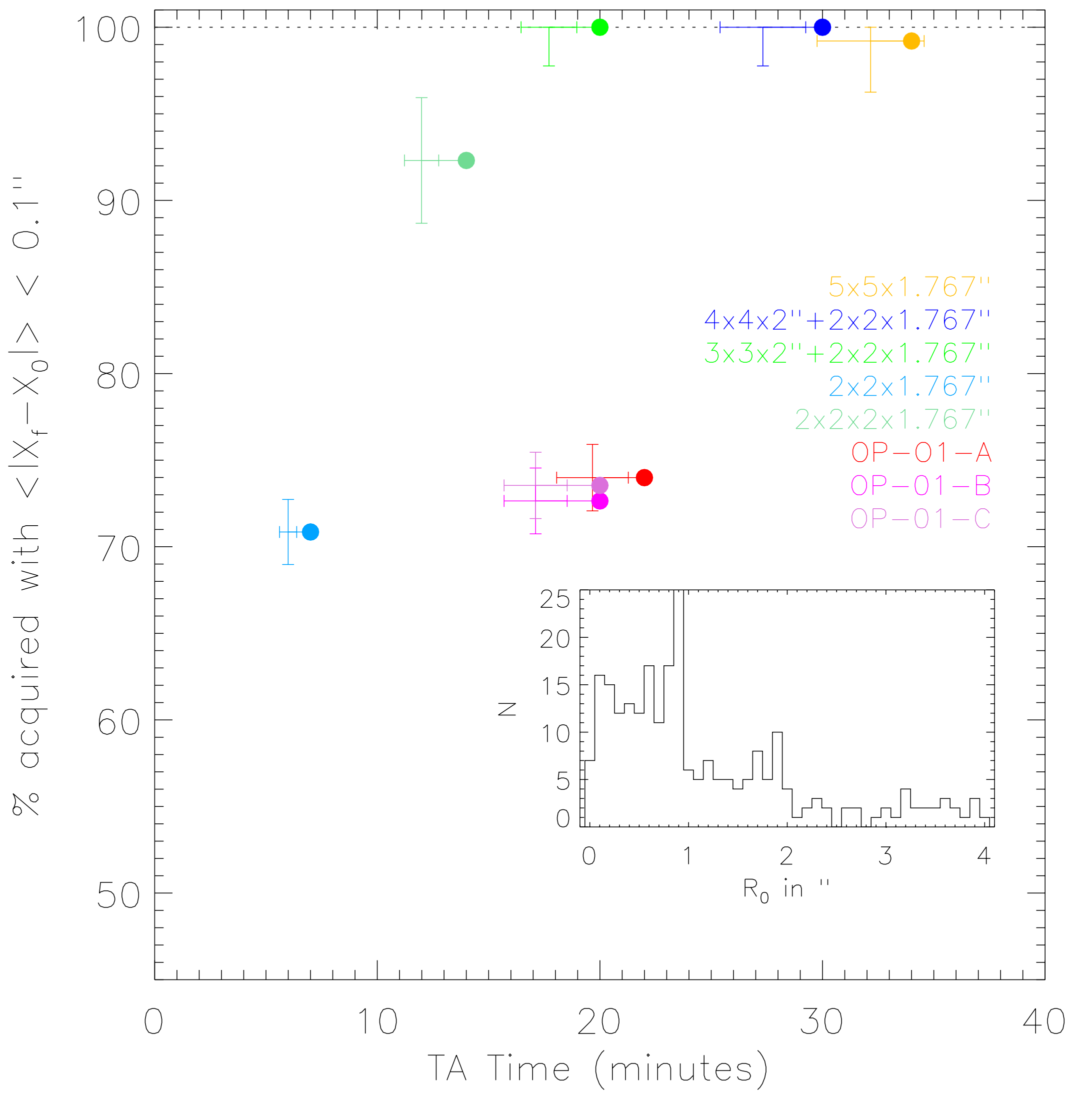

Figure 34: TA strategy summary for a 3σ=3" distribution. Left axis gives the percentage of targets acquired to within 0.1" in the DD for the distribution shown in the inset histogram (R_0<3"). Bottom axis gives the predicted total TA time in minutes. Horizontal error bars represent the temporal extent for the FUV gratings. Solid colored circles indicate the maximum expected TA time using our conservative estimates. Vertical error bars are based on the square root of the number of trials. The ideal TS strategy would be in the upper left.

6.2 COMPARISON OF TA STRATEGIES FOR A 3σ=1" DISTRIBUTION.

In many situations, the COS observer will know the coordinates of their target to within an arcsecond. In this case, many of the TA strategies of the previous section would waste valuable telescope time searching blank sky. To determine the optimum TA strategy in the 3σ=1" initial pointing error case, eight TA scenarios were tested against a population of initial pointing errors that was a combination of a Gaussian 3σ=1" distribution, plus a more uniform (4σ) component of approximately equal strength to build up number statistics at higher initial pointings errors. The DD distribution of initial target positions is shown in Figure 37. The eight scenarios tested were:

1) A 3x3x1.767" LTASRCH,
2) A 3x3x1.767" LTASRCH followed by a 2x2x1.767" LTASRCH,
3) A 2x2x1.767" LTASRCH,
4) A 2x2x1.767" LTASRCH followed by a 2x2x1.767" LTASRCH,
5) A 2x2x1.767" LTASRCH followed by a LTAPKXD followed by a 3x1.2" LTAPKD (2x2x1.767"+XD+iDD),
6) A 3x3x1.767" LTASRCH followed by a LTAPKXD followed by a 5x0.6" LTAPKD (OP-O1-A),
7) A 3x3x1.767" LTASRCH followed by a LTAPKXD followed by a 3x1.2" LTAPKD (OP-O1-B), and
8) A 3x3x1.767" LTASRCH followed by a 3x1.2" LTAPKD followed by a LTAPKXD (OP-O1-C). Again, this strategy is designed to test whether the order of the XD and DD TA phases was important.

The cumulative distribution results of these simulations are presented in Figure 35, which has identical axes to Figure 32. Again, the inset plot gives the actual initial pointing distribution (X_0 vs. Y_0), and the 3σ (1") radius is shown in red. As shown in this figure, all of eight scenarios align the target in XD direction to within 0.1" greater than 99% of the time, except the 2x2x1.767" scenario (90%). The OP-O1 derivatives are better than the LTASRCH only scenarios in XD alignment (essentially 100% to within 0.05"). The 3x3x1.767"+2x2x1.767" strategy is only slightly worse than the OP-01 derivations, achieving $\langle|Y_f-Y_0|\rangle < 0.05"$ in 95% of the cases. In the DD, the double spiral searches are better than the OP-O1 derivative scenarios in centering the target in the aperture. In the DD, all strategies except the 2x2x1.767", 2x2x1.767"+XD+iDD, and 3x3x1.767" algorithms achieved 100% pointing accuracies of $\langle|X_f-X_0|\rangle < 0.1"$. The 3x3x1.767" strategy achieved this pointing accuracy ~98% of the time.

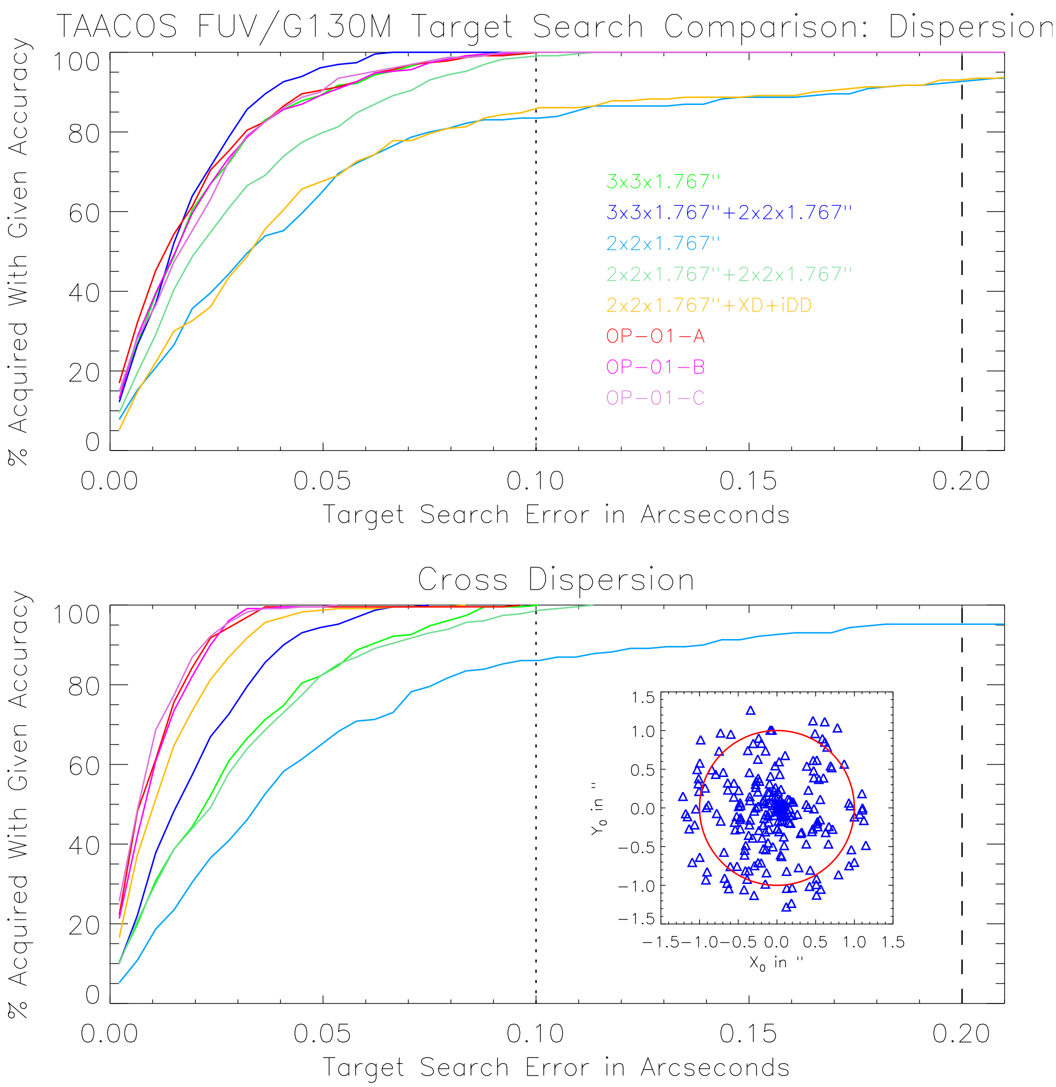

Figure 35: Comparison of TA strategies for a 3σ=1" distribution. The TA's were simulated for an $F_\lambda = 10^{-15}$ ergs/cm^2/s/Å QSO acquired with the G130M. The left axis gives the percentage of TA's which achieve $\langle|X_f-X_0|\rangle$(top, DD) and $\langle|Y_f-Y_0|\rangle$ (bottom, XD) within the target search error indicated by the bottom axis in arcseconds. These cumulative distributions indicate the overall TA accuracies as measured by TAACOS. The sky distribution of initial target positions is shown in the inset plot. The 3σ=3" area is indicated by the red circle.

To test the spatial extent of the various TA strategies, Figure 33 displays the radial accuracy extents of the eight tested TA strategies for the 3σ=1" distribution in a fashion identical to Figure 36. The results are smoothed by a 0.1" moving boxcar filter. In most cases, the recovery rates are the same (100%), so some strategies are difficult to track. As expected, all TA strategies fall off in centering accuracy as the initial pointing error exceeds the offset where the HST PSF no longer yields any counts in the LTASRCH dwell point search pattern. Most strategies tested performed well out to 0.7" initial pointing offsets. Only the 3x3x1.767"+2x2x1.767" strategy recovered 100% of the trials to within 0.1" in both XD and DD.

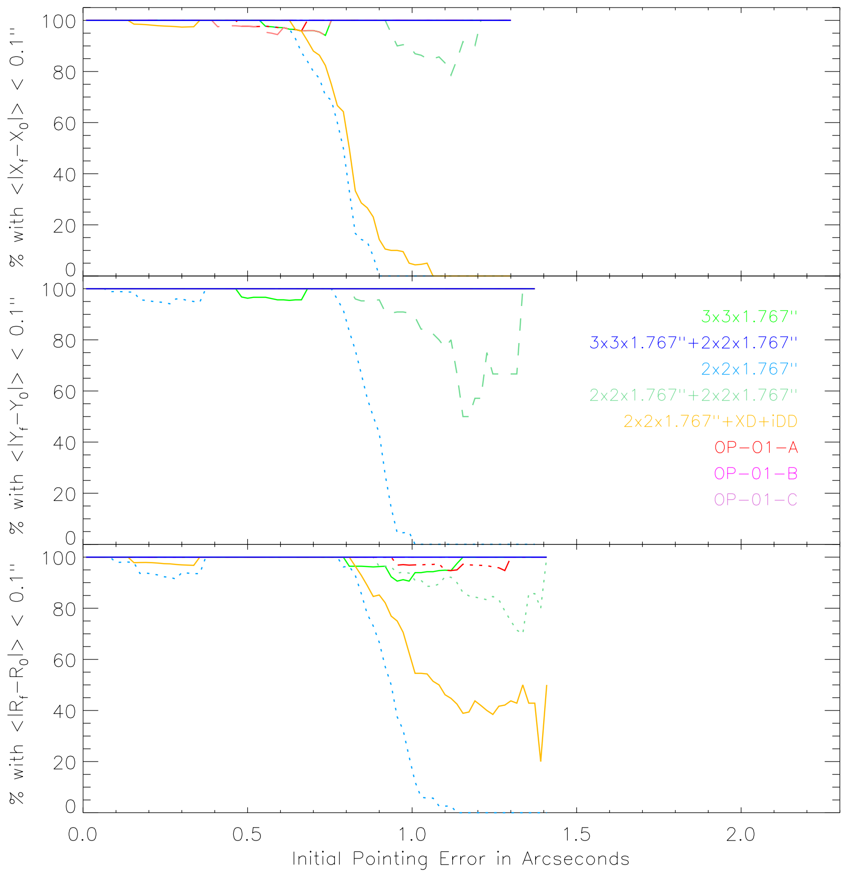

Figure 36: Radial accuracy extents of the TA strategies for a 3σ=1" distribution The left axis gives the percentage of targets acquired to within 0.1" for DD (top), XD (middle) and in radius (R, bottom). A one arcsecond moving box has been used to smooth the data. The DD and XD distribution of initial target positions (X_0 and Y_0) is shown in Figure 35, while the radial (R_0) distribution is shown in Figure 37.

Since the DD centering accuracy is the important science driver, in Figure 35 we plot the percentage of TAs that achieve ‹|X_f-X_0|› < 0.1” versus the total elapsed time. The axes, symbol meanings, and error bars are identical to those of Figure 35. The initial radial (R_0) distribution is shown as the inset histogram. Only pointings with R_0< 1” were considered. In this figure, the OP-O1-B and -C strategies are identical, indicating that the order of the XD and DD peakups is inconsequential. For this initial distribution, the best TA strategies appear to be the 2x2x1.767”+2x2x1.767” LTASRCH (12.5 minutes), the 3x3x1.767” (12 minutes), and the 2x2x1.767”+XD+iDD (12 minutes). However, the accuracy of these strategies falls off drastically if the initial pointing error exceeds 1”. If minimizing elapsed time is a priority over assurance that the target is well centered, the 2x2x1.767” LTASRCH (7 minutes) is an ideal alternative. If absolute assurance that the target is well centered is more important, then the 3x2x2x1.767” plus 2x2x1.767” LTASRCH and the OP-01-B(C) strategies are good alternatives, but require an additional 6 minutes.

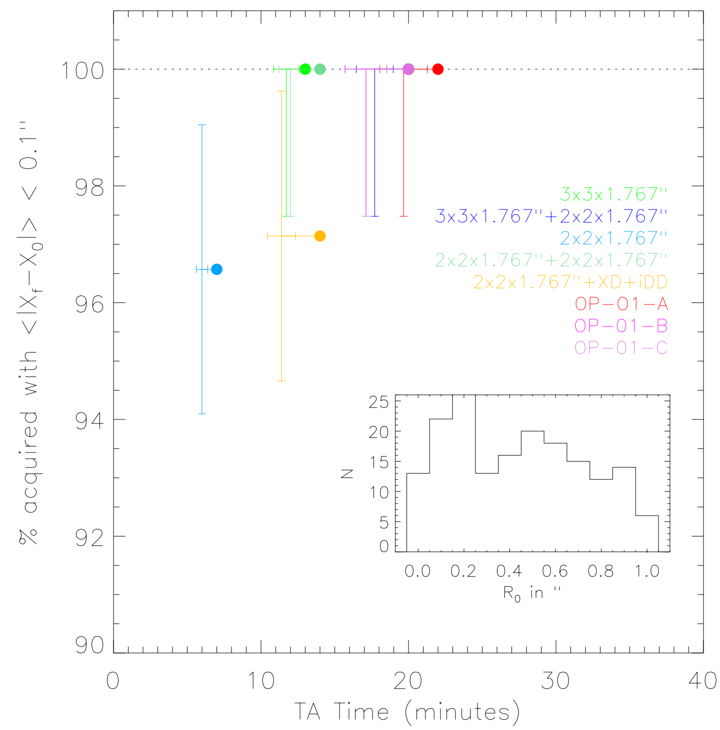

Figure 37: TA strategy summary for a 3σ=1” distribution. Axes, symbols, and error bars are identical to Figure 34. The radial distribution is shown in the inset histogram (R_0<1”).

7. SUMMARY

The goal of the TAACOS FUV project was to determine if the proposed target acquisition (TA) algorithms were sufficient to center an isolated point source in the COS PSA to within 0.3”. We find that the proposed procedures are adequate for this task, but with slight modifications, routine TAs should be able to acquire targets to within 0.1” in both dispersion (DD) and cross-dispersion (XD) in the 3σ case. As shown in Equation 1 below, this equates to a TA introduced 3σ wavelength error of <10.1 km/s for the medium resolution gratings, and <65 km/s for the G140L. TAs should take less than 30 minutes. Many strategies acquire most targets to within 0.05” in both XD and DD. All results described here are for a $F_\lambda=10^{-15}$ ergs/cm^2/s/Å QSO spectrum observed at S/N=40.

For initial pointing errors less than 3”, a 3x3x1.767” LTASRCH followed by a 2x2x1.767” LTASRCH appears to be the best TA strategy. This strategy should take ~18 minutes. However, for initial pointing errors larger than 3” this strategy fails to acquire targets accurately. A 4x4x1.767” LTASRCH followed by a 2x2x1.767” LTASRCH would acquire targets with initial pointing errors of up to 4.5” in about 28 minutes.

For initial pointing errors less than 1”, we find that a 2x2x1.767” LTASRCH acquires about 99% of targets to within 0.1” in XD and DD. This TA would take about 7 minutes. Following this LTASRCH with a second 2x2x1.767” LTASRCH or a LTAPKXD plus a LTAPKD (3x0.6”) acquires 100% of targets to within 0.1” in XD and DD. These second phases would add an additional 6 minutes to the TA time.

We find that flux-centroiding is the best method for the LTASRCH and LTAPKD phases. Using the mean cross-dispersion coordinate is sufficient in LTACAL and LTAPKXD.

Extraction subarrays that remove Geocoronal airglow lines are essential for TA. We do not see a need for moving extraction subarrays, which account for the motion of the target spectrum in the DD with motion in the aperture.

Equation 1: Velocity equivalents of 0.1” TA errors

$$\Delta v(G130M@1300Å) = c * \frac{\left(0.1'' * 43.5p/'' * 6\mu m/p * 300Å/179mm\right)}{1300Å} = 10.1 km/s \quad (0.045Å)$$

$$\Delta v(G160M@1600Å) = c * \frac{\left(0.1'' * 42.9p/'' * 6\mu m/p * 370Å/179mm\right)}{1600Å} = 10.0 km/s \quad (0.055Å)$$

$$\Delta v(G140L@1800Å) = c * \frac{\left(0.1'' * 45.4p/'' * 6\mu m/p * 1202Å/85mm\right)}{1800Å} = 64.2 km/s \quad (0.4Å)$$